CrossMark

J. Fluid Mech. (2018), *vol.* 848, *pp.* 592–630. © Cambridge University Press 2018
doi:10.1017/jfm.2018.376

Parametric study and scaling of jet manipulation using an unsteady minijet

A. K. Perumal[1] **and Y. Zhou**[1,2,†]

[1]Shenzhen Graduate School, Harbin Institute of Technology, Shenzhen, 518055, China

[2]Digital Engineering Laboratory of Offshore Equipment, Shenzhen, China

(Received 24 October 2017; revised 22 March 2018; accepted 30 April 2018;
first published online 8 June 2018)

A parametric study is conducted for the control of a turbulent jet using a single unsteady minijet. A number of control parameters that influence the decay rate K of the jet centreline mean velocity are investigated, including the mass flow rate ratio C_m, excitation frequency ratio f_e/f_0 and exit diameter ratio d/D of the minijet to main jet, along with the duty cycle (α) of the minijet injection. Extensive hot-wire, particle image velocimetry and flow visualization measurements were performed in the manipulated jet. Various flow structures have been identified, such as the flapping flow, non-flapping flow and that showing a manipulable thrust vector, depending on C_m, f_e/f_0 and α. Empirical scaling analysis unveils that, prior to the minijet impingement upon the wall of the nozzle and the generation of turbulence, the relationship $K = g_1$ (C_m, f_e/f_0, d/D, α) may be reduced to $K = g_2$ (ξ), where g_1 and g_2 are different functions and the scaling factor $\xi = (\sqrt{MR}/\alpha)(d/D)^n$ ($\sqrt{MR} \equiv C_m(D/d)$ is the momentum ratio and n is a constant that depends on α) is physically the effective momentum ratio per pulse or effective penetration depth. Discussion is conducted based on $K = g_2$ (ξ), which provides important insight into the jet control physics.

Key words: flow control, jets, scaling analysis

1. Introduction

Jet control finds important applications in thrust augmenting ejectors, thrust vector control, noise reduction, metal deposition, gas dynamic lasers, pollutant disposal, sprays, etc. Like other shear layers, the key to controlling either actively or passively entrainment and mixing processes in a jet is to manipulate the large-scale coherent structures. These structures play an important role in the dynamics of free shear flows (Brown & Roshko 1974) and, formed near the nozzle boundaries in the case of a jet, dictate the initial growth of the jet (Roshko 1976; Namer & Otugen 1988). They are sensitive to initial conditions (e.g. the boundary layer thickness, turbulence level, geometric modifications) and external periodic disturbances (Vlasov & Ginevskiy 1974), thus opening up possibilities for efficient jet control.

Previous research and development have led to numerous technologies for jet mixing control. Jet control can be active or passive. Passive control relies on the

† Email address for correspondence: yuzhou@hit.edu.cn

https://doi.org/10.1017/jfm.2018.376 Published online by Cambridge University Press

modification of geometry and does not require any additional power source. Passive techniques such as tabs (e.g. Bradbury & Khadem 1975), non-circular nozzles (e.g. Husain & Hussain 1983) and chevron nozzles (e.g. Alkislar, Krothapalli & Butler 2007; Zaman, Bridges & Huff 2011) are highly effective, although carrying with them certain penalties, for example, thrust loss, drag, practical constraints (e.g. Gutmark & Grinstein 1999). On the other hand, active methods require the input of external power, e.g. acoustic excitation (e.g. Zaman & Hussain 1981), vibrating ribbons (e.g. Zaman & Hussain 1981), piezo-electric actuators (e.g. Wiltse & Glezer 1993; Parekh *et al.* 1996), plasma actuators (e.g. Samimy *et al.* 2007), synthetic jet (e.g. Tamburello & Amitay 2007) and flip-flop jets (Raman, Hailye & Rice 1993). However, the additional power requirement and weight to achieve the required effect have so far precluded any significant interest in active control (Knowles and Saddington 2006).

Recently, one active technique has attracted considerable attention in the literature, which uses a minijet, also referred to as the secondary jet, fluidic means or air-tab, as the actuator. This technique can be easily adapted to the flow conditions and will not cause thrust loss (e.g. Yu *et al.* 2008); additionally, the penalty in increased weight, cost and mechanical complexity is also reduced, compared with many other techniques such as non-circular nozzles, acoustic excitations. In fact, the minijet can be turned on and off depending on practical needs and this has encouraged many researchers to explore this option for jet mixing and noise control. The concept to use fluidic injection for enhancing jet mixing was first proposed by Davis (1982) on a Mach 0.8 jet. The steady minijets have been used to manipulate the subsonic (e.g. Wan & Yu 2013), sonic (e.g. Kumar, Verma & Rathakrishnan 2015) and supersonic jets (e.g. Chauvet, Deck & Jacquin 2007). This technique may reproduce the same benefits of the solid tabs (e.g. Behrouzi, Feng & McGuirk 2008; Yu *et al.* 2008).

The minijet injection can be significantly more efficient if made pulsed (e.g. Freund & Moin 2000; Ibrahim, Kunimura & Nakamura 2002). The primary reason why the unsteady injection is more effective than the steady is twofold. First, given the same mass flow rate, the unsteady injection is associated with a higher momentum than the steady (Bons, Sondergaard & Rivir 2001; Cattafesta & Sheplak 2011), thus penetrating deeper into the primary jet than the steady counterpart (Lardeau, Lamballais & Bonnet 2002) and producing a more profound influence on the large-scale structures (New & Tay 2004). Second, the periodic excitation may capitalize on the inherent instabilities of the main flow (Seifert, Darabi & Wyganski 1996). Previous investigations on jet control using unsteady fluidic means are mostly focused on the mass flow rate and frequency ratios, i.e. C_m and f_e/f_0, of the minijet to main jet (e.g. Parekh *et al.* 1996; Ibrahim *et al.* 2002; Behrouzi *et al.* 2008 and Yang *et al.* 2016), where f_e and f_0 are the excitation frequency of the unsteady minijet and the preferred-mode frequency of the main jet, respectively. Raman & Cornelius (1995) and Raman (1997) manipulated a rectangular jet at a Reynolds number of 10^5 using two unsteady fluidic actuators. Their subharmonic excitation ($f_e/f_0 = 0.5$) at $C_m = 2.4\,\%$ produced a 35 % reduction in the potential core length and a 60 % increase at $x^* = 3.0$ in the normalized mass flux, compared with the unforced jet. In this paper, an asterisk denotes normalization by the nozzle exit diameter D and/or time-averaged exit velocity $\bar{U}_j$ of the main jet. Kamran & McGuirk (2011) noted that the unsteady injection made the jet cross-section highly asymmetric, like an elliptic jet, enhancing near-field mixing. Yang & Zhou (2016) and Yang *et al.* (2016) conducted detailed investigations on the effect of C_m and f_e/f_0 on a turbulent round jet ($Re = 8000$) manipulated by two symmetrically or asymmetrically arranged unsteady minijets, respectively. Three types of coherent structures were identified under the symmetric excitation, i.e. the contorted ring vortices, two pairs

https://doi.org/10.1017/jfm.2018.376 Published online by Cambridge University Press

of streamwise vortices and mushroom-like counter-rotating structures which were sequentially 'tossed' out radially in the non-injection plane and produced a larger spread than in the injection plane. On the other hand, the asymmetric excitation produced a flapping jet column along the injection plane, resulting in a 30 % higher decay rate in the jet centreline mean velocity than the symmetric counterpart.

Previous studies have improved tremendously our understanding of jet control based on unsteady minijets. Nevertheless, a systematic parametric study in this area is missing in the literature. For instance, there is another parameter, namely the duty cycle α, associated with unsteady minijets, that is available for optimizing the control performance (e.g. Johari, Pacheco-Tougas & Hermanson 1999; Bons *et al.* 2001). There has been so far no study on its influence on the jet control performance (Kamran & McGuirk 2011). Furthermore, the effect of the diameter ratio d/D, where d is the minijet exit diameter, has not been thoroughly understood either although Davis (1982) pointed out a decrease in d/D may improve the control efficiency. Naturally, a number of questions arise. How do α and d/D influence jet control based on unsteady minijet? Is there any interesting flow physics behind possible effective and efficient control? Realizing jet entrainment or mixing may depend on C_m, f_e/f_0, α and d/D, *viz.* the decay rate of the jet centreline mean velocity $K = g$ (C_m, f_e/f_0, α, d/D), we are faced yet another important issue, that is, could we obtain from C_m, f_e/f_0, α and d/D the similarity variables that reflect the physical essence of the jet control and can be used to design minijet in full-scale practical applications? Could we find a scaling factor ξ so that $K = g_1$ ($C_m, f_e/f_0, \alpha$, d/D) may be reduced to $K = g_2$ (ξ), where g_1 and g_2 are different functions? This may have a profound impact upon possible practical applications since the flow structure and the similarity parameters obtained from a laboratory-scale model are the same as those of a full-scale model (e.g. Wickersham 2007).

This study sets out to address the above issues raised. A turbulent axisymmetric jet is experimentally manipulated using a single unsteady minijet. Extensive measurements are conducted using hot-wire, smoke flow visualization and particle image velocimetry (PIV) in three orthogonal planes of the manipulated jet. The paper is organized as following. Experimental set-up and measurement details are given in § 2. Section 3 deals with the general characteristics of the unperturbed jet and the minijet-produced flow. The dependence of K on d/D, $C_m, f_e/f_0$ and α is discussed in § 4. Section 5 introduces the empirical scaling analysis based on experimental data. This work is concluded in § 6.

2. Experimental details

2.1. *Test facilities*

The experimental rig is deployed in a spacious air-conditioned laboratory whose room temperature is maintained to be constant with a maximum variation of $\pm 0.5\,^{\circ}\mathrm{C}$. The rig is centrally placed in an area of around 4.5 m in width and 4.0 m in height. The nearest wall from the nozzle exit is 7.0 m away from the nozzle exit, well above $70D$ required for neglecting the wall effects (Malmstrom *et al.* 1997). Careful measures are taken to ensure no external disturbance to the flow by any means during experiments since the jet is highly sensitive to the background noise (Hussain 1986).

The rig consists of a main jet and a minijet assembly (figure 1). The compressed air for the main or primary jet and minijet comes from three air tanks connected in series, with a total storage capacity of 8 m^3 and a pressure of 12 MPa, which is sufficient for 3 h in running time. The air supply to the main jet and the minijet is controlled

https://doi.org/10.1017/jfm.2018.376 Published online by Cambridge University Press

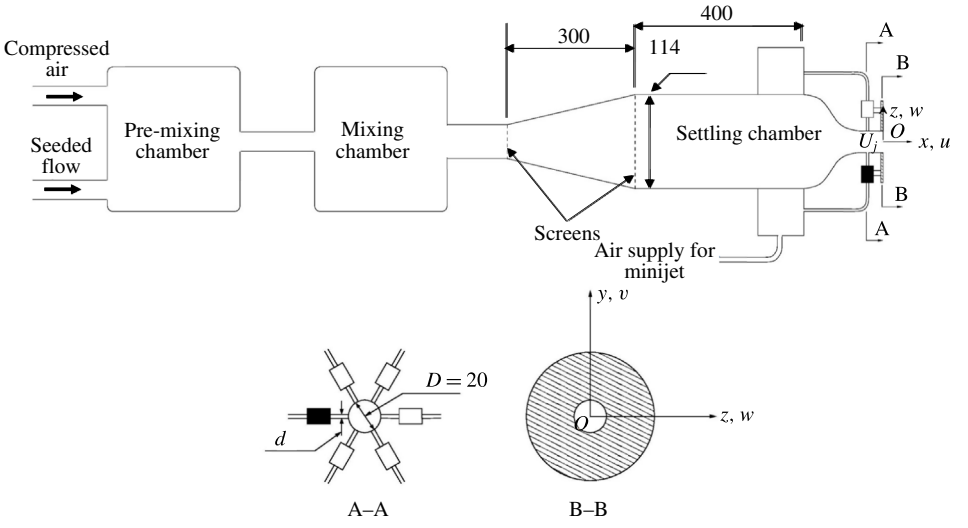


FIGURE 1. Schematic of experimental rig, minijet assembly and the definition of the coordinate system.

by separate valves. The compressed air is mixed with seeding particles in the pre-mixing and mixing chamber in the case of PIV or flow visualization measurements and then enters a plenum chamber, consisting of a 300 mm long diffuser of 15° in half-angle and a 400 mm long cylindrical settling chamber with an inner diameter of 114 mm. The flow goes through two wire-mesh screens before entering into the smooth contraction nozzle. The profile of the nozzle contraction is identical to that used in Yang & Zhou (2016). The contraction is extended with a 47 mm long smooth tube, whose inner diameter is the same as the nozzle exit diameter D (= 20 mm).

The main jet nozzle is drilled with six holes of diameter d, separated azimuthally by 60° and located 17 mm upstream of the main jet exit. Three nozzles, $d = 0.5$, 0.8 and 1.0 mm, respectively, are made and exchangeable. Each hole is connected via a short plastic hose to an electromagnetic valve (Koganei K2-100SF-09-LL) with its maximum frequency of 1 kHz, which is used to generate unsteady minijet. The 6 electromagnetic valves are controlled independently. In this study, only one single minijet is used, which is shaded in figure 1. The valve is driven by a square-wave voltage signal of 0–5 V from the output board of a NI system and its α may vary from 0.1 to 1.0. The square wave excitation is more effective than sinusoidal forcing (M'Closkey *et al.* 2002). The f_e and α of the minijet can be adjusted by changing the frequency and duty cycle of the square-wave signal. The frequency range that can be achieved is 0–1 kHz. Mass flow rates of both main jet and minijet are adjustable independently via two separate mass flow meters, whose measurement uncertainty is no more than ±1 %.

The coordinate system (x, y, z) and its origin O are defined in figure 1. Measurements were conducted in the minijet injection (x–z) plane, the orthogonal or non-injection (x–y) plane and at a number of cross-sectional planes (y–z) of the main jet. The instantaneous velocities are denoted by U, V and W along x, y and z, respectively, and their fluctuating components are given by u, v and w, respectively.

https://doi.org/10.1017/jfm.2018.376 Published online by Cambridge University Press

2.2. *Flow measurements and data processing*

U is measured using a single tungsten wire of 5 μm in diameter, operated on a constant temperature circuit (Dantec Streamline) at an over-heat ratio of 1.8. The signal from the wire is offset, filtered at a cutoff frequency of 3 kHz, amplified and then digitized using a 12-bit A/D board at a sampling frequency of 6 kHz. The record duration is 80 s, which ensures that u_{rms} is converged to within 1 % uncertainty, where subscript *rms* denotes the root mean square value. The hot-wire probe is mounted on a computer-controlled three-dimensional traversing mechanism, whose streamwise and transverse resolutions are 0.01 mm. The hot-wire signal is calibrated based on the streamwise mean velocity measured using a standard Pitot static tube with an outer diameter 2.2 mm, connected to an electronic micro manometer (Furness FCO510) and placed, side by side with the hot-wire, parallel to the flow near the centre of the nozzle exit. The Pitot static probe may read a lower value in an open jet of limited diameter as compared to an infinite stream, due to flow acceleration. The present blockage ratio, i.e. the ratio of the probe tip area to the nozzle exit area, is 1.2 %, smaller than the threshold of 5 %, exceeding which the blockage may incur a considerable effect on pressure and hence flow velocity measurements (Chue 1975).

Flow visualization and particle imaging velocimetry (PIV) measurements are performed using a time-resolved Dantec standard PIV2100 in the injection and non-injection planes and also at various cross-sectional planes of the main jet. A TSI oil droplet generator (TSI 9307-6) is used to generate fog for seeding the flow. The seeding particles have a diameter of approximately 1 μm and are thus adequate for tracking turbulent or high-speed gas flows (Melling 1997). The seeding particles, injected into the upstream mixing chamber, are homogeneously distributed in the main jet. Flow illumination is provided by a laser sheet of 1 mm thick generated from two standard pulsed laser sources (Beam Tech 500-10) with 532 nm wavelength and a maximum energy output of 30 mJ per pulse. The flow images are captured at a framing rate of 540 images per second using one HiSense MkII CCD camera (double frames, 2048 × 2048 pixels). The Dynamic Studio v3.41 is used to synchronize flow illumination and image capturing during measurements.

In flow visualization and velocity measurements in the x–z and x–y planes, the captured image covers an area of $x^* = 0$–10 and y^* or $z^* = -5 \sim +5$. The longitudinal and lateral image magnifications are identical, 0.09 mm pixel^{-1}. The time interval between two consecutive laser pulses is chosen as 75 μs, during which a particle could travel only 0.05 mm (4 pixels or $0.003D$). In post-processing, a built-in adaptive correlation function of the Flow Map Processor (PIV 2001 type) is used with an interrogation window of 32 × 32 pixels and a 75 % overlap along both directions, thus producing 253 × 253 velocity vectors. The total number of images captured is 1500 pairs. It has been confirmed that the centreline mean velocity distribution calculated from snapshots of the flow field collapses already very well with the hot-wire data.

In the measurements of the flow in the y–z plane, the laser sheet thickness is set at approximately 3 mm, following Huang, Zhou & Zhou (2006). Similarly to Yang & Zhou (2016), the camera is placed at $50D$ downstream from the light sheet so that the interference of the camera on the measurement is negligibly small. The image magnification is 0.09 mm pixel^{-1} so that not only the flow field of interest is adequately covered but also the image resolution is maximized. As the axial velocity component is much larger than the two transverse components, the seeding particles could cross the 3 mm thick light sheet if the time interval between two consecutive images is large, thus causing poor correlation (Huang, Dabiri & Gharib 1997; Pattenden, Turnock & Zhang 2005). Thus, the time interval for the present case

https://doi.org/10.1017/jfm.2018.376 Published online by Cambridge University Press

is chosen to be 25 μs, which is found to yield satisfactory results. The number of velocity vectors is the same as that in the (x–y) and (x–z) planes. The total number of flow images captured is again 1500 pairs for each set of PIV data.

Experiments were conducted for a jet Reynolds number $Re \equiv \bar{U}_j D/\nu$ of 8000, where ν is the kinematic viscosity of air. Following Zhou *et al.* (2012) and Yang & Zhou (2016), $K = (\bar{U}_j - \bar{U}_{5D})/\bar{U}_j$ is used to evaluate the jet entrainment rate, where $\bar{U}_{5D}$ denotes the jet centreline mean velocity at $x^* = 5$. The choice of K is based on the following considerations. Firstly, it has been demonstrated in Zhou *et al.* (2012) that thus defined K is correlated approximately linearly with an equivalent jet half-width $R_{eq} = [R_H R_V]^{1/2}$, where R_H and R_V are the jet half-widths in two orthogonal planes, that is, K is directly connected to the entrainment rate of the manipulated jet. Secondly, as documented by Fan *et al.* (2017), the difference ΔK between the K values with and without control reaches a maximum at $x^* \approx 5$ (their figure 7), that is, the K estimated based on the streamwise velocity measured at $x^* = 5$ is most sensitive to the change in the control parameters. Thirdly, the variation in K is almost linear from $x^* = 0$ to $x^* \approx 7$ under control (figure 7, Fan *et al.* 2017), that is, a single value of K may be used to describe reasonably well the jet decay rate in the near field under control. This is as Breidenthal *et al.* (1985) did, who used an aspirating probe to measure the concentration fluctuation c of two mixing streams (a rectangular duct flow and a transverse jet) and reported that the decay rate of the root mean square value c_{rms} of the concentration fluctuation was approximately linearly connected to the momentum ratio (J) of the transverse jet to the rectangular duct flow. This linear relationship persisted over $1 < x^* < 10$ (see their figure 5). Therefore, they used a single decay rate of c_{rms}, measured at $x^* = 8.9$, to characterize the mixing of the two streams and suggested that this decay rate provided a measure for the mixing efficacy of turbulence. So does K in the context of the present work.

3. Initial conditions of flow under minijet injection

In the absence of any perturbation, $\overline{U}^*$ measured at $x^* = 0.05$ exhibits a 'top-hat' profile (not shown) and the corresponding $u^*_{rms} = u_{rms}/\bar{U}_j$ is 0.3 %. The power spectral density functions E_u of u measured on the centreline over $x^* = 2$–6 exhibit a pronounced peak at $f_0 = 135$ Hz, suggesting the occurrence of preferred-mode structures. The figure that shows the preferred mode was presented in Yang & Zhou (2016), and is thus not included in this article. The corresponding Strouhal number St ($\equiv f_0 D/\bar{U}_j$) is 0.45, falling in the expected range of 0.24–0.64 for a natural jet (e.g. Crow & Champagne 1971; Gutmark & Ho 1983).

It is important to document how the unsteady minijet changes the initial conditions of the main jet, which is crucial for understanding the flow physics behind jet control results. Following Zhou *et al.* (2012), we placed a single hot-wire upstream of the main jet exit at $x^* = -0.85$ ($y^* = 0$ and $z^* = -0.35$), where the minijet is excited at $\alpha = 0.1$, 0.4 and 0.7 ($C_m = 0.5$ %, $f_e/f_0 = 0.5$). The hot-wire is oriented normally to both minijet and main jet axes, thus capturing the W signal (figure 2*a*) in the absence of the main jet or both U and W in the presence of the main jet ($\bar{U}_j = 6$ m s^{-1}). In the absence of the main jet, the W^* signal (figure 2*a*) exhibits very distinct behaviours as α varies, where $W^* = 0$ and significantly above 0 correspond to the off- and on-states of the minijet, respectively. Given $C_m = 0.5$ % and $f_e/f_0 = 0.5$, W^* displays sharp peaks in the on-state, which are periodic and clearly separated for $\alpha = 0.1$. However, the peaks appear less pronounced at $\alpha = 0.4$ and 0.7; furthermore, the on-states are not so neatly separated at $\alpha = 0.7$. It seems that for $\alpha \geqslant 0.7$ the off-state is temporally very

https://doi.org/10.1017/jfm.2018.376 Published online by Cambridge University Press

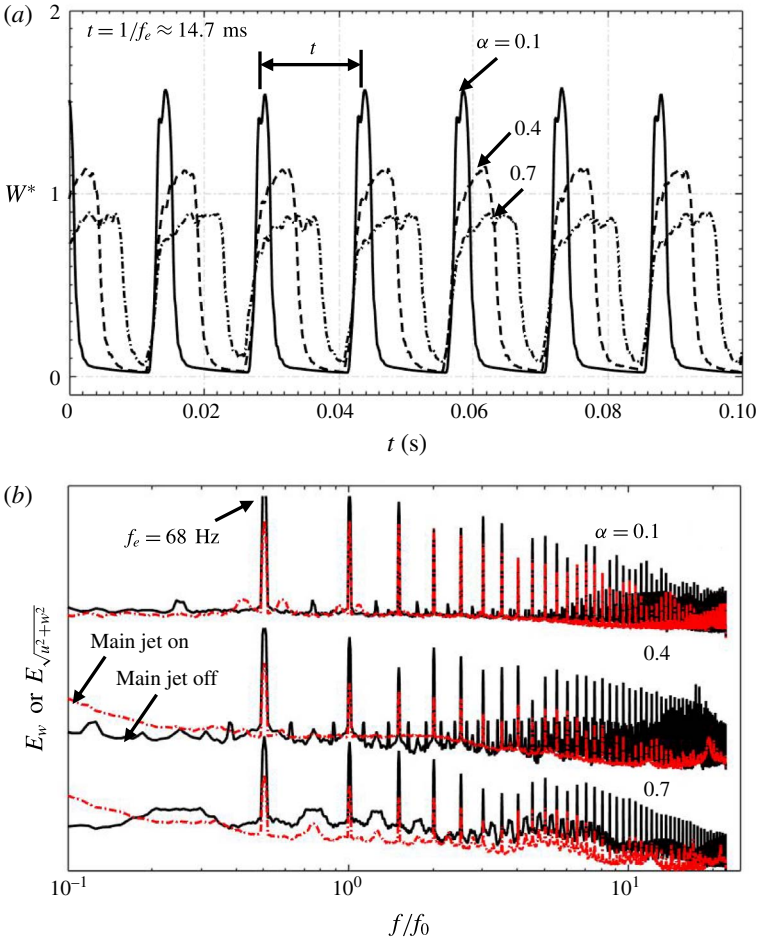


FIGURE 2. (Colour online) (*a*) Time histories measured when the main jet is not operated. (*b*) Power spectral density functions of streamwise fluctuating velocity w in the absence of the main jet or $\sqrt{u^2+w^2}$ in the presence of the main jet, measured at $(x^*, y^*, z^*) = (-0.85, 0, -0.35)$ for $C_m = 0.5\,\%$, $f_e/f_0 = 0.5$ and $d/D = 1/20$.

limited in duration, compared to the on-state, and the excitation may actually behave closely like a quasi-steady control jet. The more pronounced peak in W^* for $\alpha = 0.1$ than for $\alpha = 0.4$ or 0.9 implies a higher penetration depth at smaller α, as reported by Johari *et al.* (1999) for the pulsed jet in cross-flow. It is worth commenting that the actual duty cycle experienced in excitation may be slightly larger than the input duty cycle, as specified by an NI board, due to the fact that, even after closing the valve, there may be some fluid flowing through the tube that connects the valve and nozzle (Sailor, Rohli & Fu 1999; M'Closkey *et al.* 2002). In fact, the waveform observed at the output of the minijet is not really square although a great effort has been made to reduce the connection tube length between the valve and injection point to the minimum, confirming that the output or actual duty cycle may not exactly equal the input duty cycle. Apparently, the penetration depth depends on both C_m and α.

E_w or $E_{\sqrt{u^2+w^2}}$ is qualitatively the same with or without the main jet operated, displaying pronounced peaks at f_e/f_0 and its harmonics (figure 2*b*) in both cases.

https://doi.org/10.1017/jfm.2018.376 Published online by Cambridge University Press

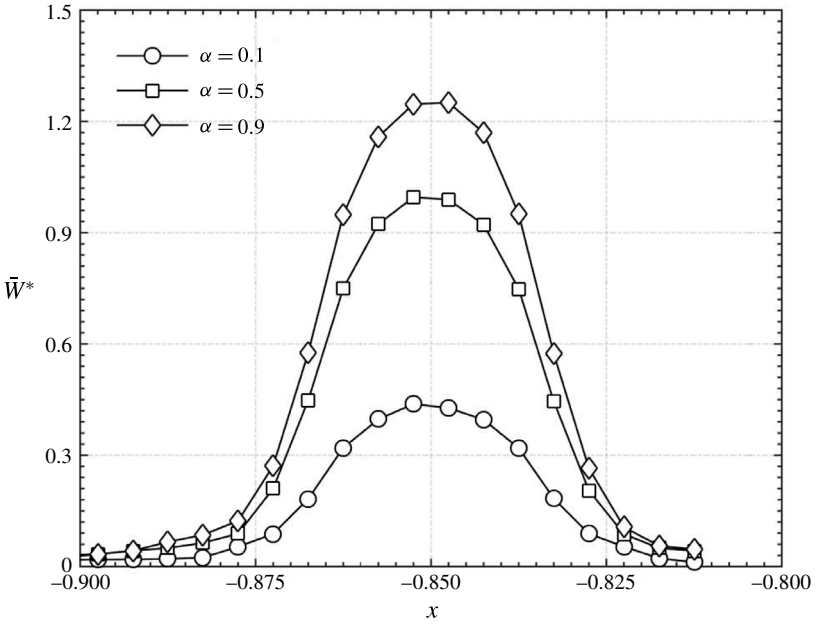


FIGURE 3. Time-averaged velocity profiles of the minijet measured at $(y^*, z^*) = (0, -0.475)$ for $C_m = 1.0\,\%$, $f_e/f_0 = 0.5$ and $d/D = 1/20$ in the absence of the main jet.

The peaks at harmonics are due to the resonance in the nozzle (Zhou *et al.* 2012), which was referred to as the parametric resonance by Huang & Hsiao (1999). Evidently, the unsteady injection produces the periodic structures in the flow before its issue from the nozzle exit. Note from figure 2 that varying α does not affect the predominant frequencies in the spectra.

The exit velocity profile of the minijet may have an influence on the flow structure development as the parabolic profile produces a deeper penetration in the main jet than the top-hat (New, Lim & Luo 2006). To envisage this, hot-wire measurements were carried out at pre-determined minijet flow rate in the absence of the main jet at a sampling frequency of 6 kHz for 100 s. The hot-wire was located approximately at the minijet exit ($y^* = 0$, $z^* = -0.475$) and traversed, at an increment of 0.1 mm, across the minijet along the x^* direction. Figure 3 shows the measured velocity profile of the minijet for $\alpha = 0.1$, 0.5 and 0.9. A parabolic velocity profile is seen for $\alpha = 0.1$, 0.5 and 0.9. The thick shear layer of the parabolic velocity profile may cause a delay in the formation of the leading-edge and lee-side vortices, compared with the thin shear layer case associated with the top-hat velocity profile (New *et al.* 2006).

The minijet-produced structures (Yang & Zhou 2016) and their interaction with the main jet play a crucial role in the overall jet development. To understand the initial disturbance caused by the minijet injection on the main jet, figure 4 presents the radial distributions of u^*_{rms} at $x^* = 0.05$ along the injection and orthogonal non-injection directions. Note that u^*_{rms} in the orthogonal non-injection plane is presented only for $y^* > 0$, assuming a reasonably symmetric distribution of u^*_{rms} along the y direction. As a reference, the unexcited jet ($C_m = 0\,\%$) is also shown in figure 4. There is a great change in u^*_{rms} along both the z and y directions under excitation, depending on C_m. At $C_m = 0.20\,\%$, the u^*_{rms} is essentially unchanged for $z^* > 0.15$ (figure 4*a*), suggesting that the velocity disturbance produced by unsteady minijet injection is limited, leaving the

https://doi.org/10.1017/jfm.2018.376 Published online by Cambridge University Press

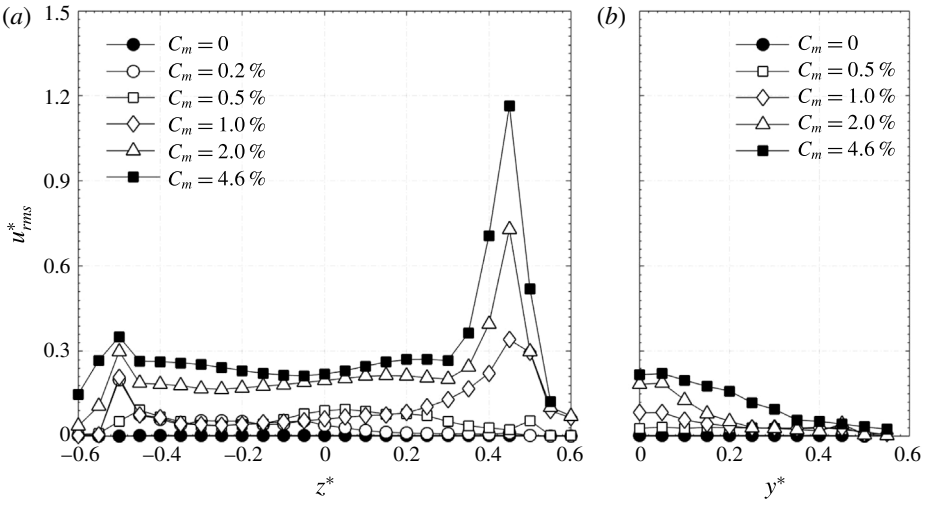


FIGURE 4. Radial distributions of $u^*_{rms} = u_{rms}/\bar{U}_j$ measured at $x^* = 0.05$ ($f_e/f_0 = 0.5$, $\alpha = 0.1$, $d/D = 1/20$): (*a*) in the *x*–*z* or injection plane, (*b*) in the *x*–*y* or non-injection plane.

shear layer at $z^* \approx 0.4$–0.5 undisturbed. With C_m increasing to 0.5 %, the u^*_{rms} displays an increase for $z^* > 0$, indicating that the minijet has penetrated through the main jet centre and perhaps the nozzle wall feels the disturbance of the minijet, as suggested by the tiny increase in u^*_{rms} at $z^* = 0.5$ (figure 4*a*). At $C_m = 1.0\,\%$, the u^*_{rms} increases significantly over $0 < z^* < 0.45$, an indication that the shear layer on the opposite side to the minijet starts to be disturbed by the injection. There is also an appreciable increase in u^*_{rms} along the y direction (figure 4*b*). Up to this stage, the flow at the nozzle exit remains to be laminar, as is evident in the hot-wire measured U signals along both y and z directions (figure 5). Note that the minijet, issuing from $z^* = -0.5$, injects along the z direction. The fluctuations in figure 5 apparently originate from the minijet injection into the main jet. There is no appreciable fluctuation in U along the y direction. At $C_m = 2.0\,\%$, the u^*_{rms} rises very significantly over $-0.6 < z^* < 0.6$ (figure 4*a*). So does u^*_{rms} around the centre along the y-direction. This is a sign that the minijet flow impinges upon the opposite wall of the main jet nozzle at $z^* = 0.5$. Nevertheless, the flow remains to be laminar or at most starts the transition, as reflected by the U signals (figure 5). At $C_m = 4.6\,\%$, u^*_{rms} rises sharply about $z^* = 0.5$ along the z-direction and meanwhile grows almost across the main jet along the y direction. The strong minijet impingement upon the wall now starts to produce turbulence; the U signals (figure 5) captured along both the y and z directions all display random fluctuations. It seems plausible that the maximum penetration depth of the minijet occurs at $C_m = 2.0\,\%$. Increasing C_m to 4.6 %, the maximum penetration remains the same as that at $C_m = 2.0\,\%$; however, the substantial rise in u^*_{rms} and the randomly fluctuating U signals over $-0.6 < z^* < 0.6$ and $0 < y^* < 0.4$ (figures 4 and 5) suggest a fully turbulent jet right from the nozzle exit.

The normalized mean velocity profiles in two orthogonal planes are illustrated in figure 6 for the perturbed jet at $C_m = 1.0\,\%$, $f_e/f_0 = 0.5$, $\alpha = 0.1$ and $d/D = 1/20$, which exhibit a reasonable symmetry about the jet centre ($y^* = 0$ or $z^* = 0$) for the x^* range examined. There is a slight deviation in the location of the maximum velocity from the geometric centre $z^* = 0$, as observed by Yang *et al.* (2016). This is primarily a result of the asymmetric injection. The difference between the maximum velocity and

https://doi.org/10.1017/jfm.2018.376 Published online by Cambridge University Press

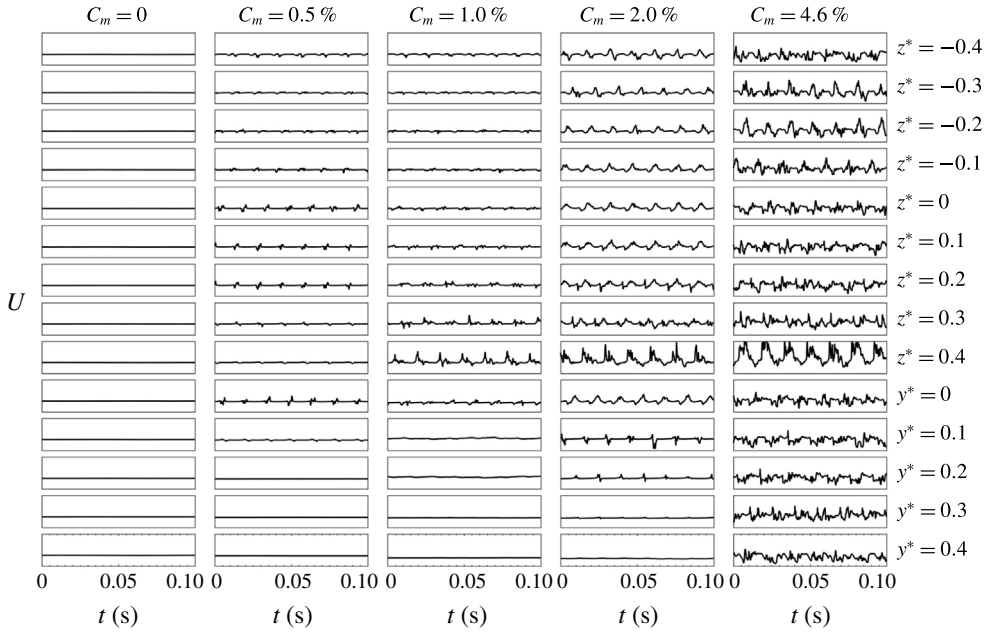


FIGURE 5. Typical signals of instantaneous streamwise U measured along the y^* and z^* direction at $x^* = 0.05$ ($f_e/f_0 = 0.5$, $\alpha = 0.1$, $d/D = 1/20$). The same scale is applied for all signals.

the velocity at $z^* = 0$ is in general very small, causing an error of no more than 1 % in K. This difference becomes appreciable only for a quasi-steady control ($\alpha \geqslant 0.9$) at $C_m > 3.5\,\%$ when the jet column deflects away from the geometric axis, which may be referred to as thrust vectoring. As a consequence, there is an artificial increase in K, which will be further discussed in § 5.

4. Parametric study of jet manipulation

In this section, we document the dependence of K on f_e/f_0, C_m, α and d/D under the minijet excitation.

4.1. *Excitation frequency ratio effect*

Figure 7 presents the dependence of K on f_e/f_0 for different C_m at $\alpha = 0.1$. The K of the manipulated jet exceeds greatly that (0.03) of the natural jet over the entire range of f_e/f_0, suggesting an effective manipulation. Its value exhibits a dependence on f_e/f_0, and may show its peak at $f_e/f_0 = 0.5$ ($f_e^* = f_e D/\bar{U}_j = 0.23$) or at $f_e/f_0 = 1.0$ ($f_e^* = 0.45$). The latter is very minor and occurs only for small C_m, i.e. 0.20 % and 0.70 %. The maximum K takes place at $f_e/f_0 = 1.0$ for $C_m \leqslant 0.2$ but at $f_e/f_0 = 0.5$ ($f_e^* = 0.23$) for $C_m > 0.2\,\%$. Freund & Moin (2000) conducted a direct numerical simulation of a Mach 0.9 jet at $Re = 3.6 \times 10^3$, which was excited at $f_e^* = 0.2$ (the subharmonic of the preferred-mode frequency) and 0.4 ($C_m = 3.5\,\%$) using two slot jets at 180° out of phase. They revealed that $f_e^* = 0.2$ produced a higher jet spread and reduced the potential core more than $f_e^* = 0.4$, that is, their subharmonic excitation was more

https://doi.org/10.1017/jfm.2018.376 Published online by Cambridge University Press

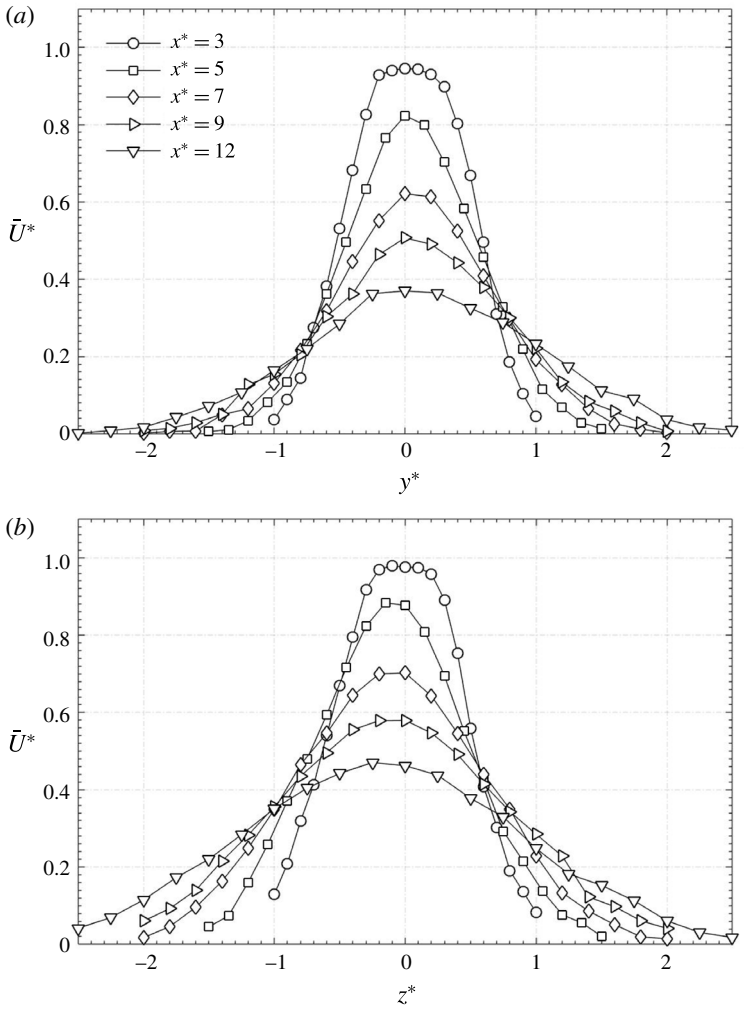


FIGURE 6. Normalized streamwise mean velocities measured along the y and z axes at different axial locations for $C_m = 1.0\,\%$, $f_e/f_0 = 0.5$, $\alpha = 0.1$ and $d/D = 1/20$.

effective than the excitation at the preferred-mode frequency. Similarly, M'Closkey *et al.* (2002) also reported that the optimal jet penetration and spread for the pulsed jet in cross-flow occurred at the subharmonic excitation of the preferred-mode structures. The effective excitation at $f_e/f_0 = 0.5$ is not surprising. Ho & Huang (1982) noted that the spreading rate of a mixing layer can be greatly manipulated at the subharmonic of the preferred-mode frequency, where many vortices merge together through the collective interaction which is distinct from the ordinary vortex merging. Nevertheless, the physical mechanism behind this observation has not been unveiled.

Insight into why the maximum K shifts from $f_e/f_0 = 1.0$ to 0.5 for $C_m > 0.2$ may be gained through examining typical photographs (figure 8) captured from flow visualization in the x–z plane of the jet, with and without manipulation. The manipulated jet depends on C_m and f_e/f_0 and appears very different from the natural jet. In general, the minijet perturbation causes an early roll up of vortices in the injection plane ($z^* \approx -0.5$, $x^* \approx 1.0$), and the jet structure is asymmetrical or staggered

https://doi.org/10.1017/jfm.2018.376 Published online by Cambridge University Press

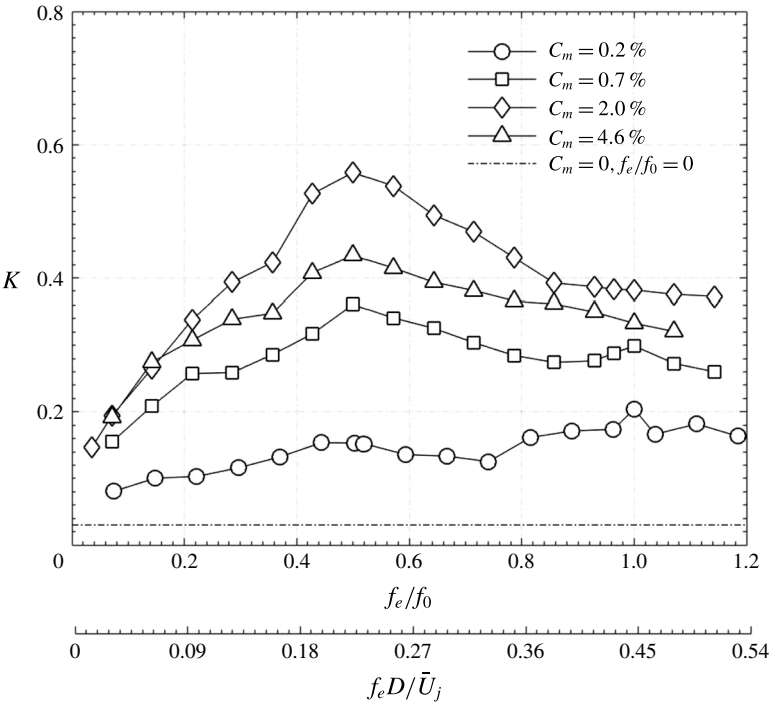


FIGURE 7. Dependence of the centreline mean velocity jet decay rate K on the excitation frequency ratio f_e/f_0 or $f_e D/\bar{U}_j$ for $\alpha = 0.1$ and $d/D = 1/20$.

in the x–z plane (figure 8*a*1–*d*2) but symmetrical in the x–y plane (not shown). At $C_m = 0.20\,\%$ and $f_e/f_0 = 0.5$ (figure 8*a*1), the perturbed jet column shows an upward movement at $x^* \approx 1.0$ and then downward at $x^* \approx 1.8$ and again upward at $x^* \approx 2.4$. Such an oscillation of the jet column is also reported by Freund & Moin (2000) and Iio *et al.* (2013) and referred to as the flapping jet column. The flapping phenomenon occurs for $f_e/f_0 = 0.5$ and 1.0 given $C_m = 0.20\,\%$ (figure 8*a*1,*a*2) but only for $f_e/f_0 = 0.5$ at $C_m \geqslant 0.70\,\%$ (figure 8*b*1,*c*1,*d*1). The subharmonic excitation ($f_e/f_0 = 0.5$) is generally characterized by inclined ring vortices, whereas the harmonic ($f_e/f_0 = 1.0$) is characterized by axial ring vortices. The minijet injection induces early roll up of the ring vortex near the injection point. Given an adequate penetration depth or C_m, one end of an inclined ring vortex may approach a neighbouring vortex, forming zigzag-like organized structures and hence starting a pairing process at the approaching ends. This strong vortex interaction or pairing induces upward motion of fluid on one side and downward motion on the other side, generating the flapping motion. This scenario is fully consistent with the observation that the flapping jet column occurs at the subharmonic excitation and at $C_m \geqslant 0.70\,\%$. A more detailed physical explanation and associated evidence for the occurrence of the flapping motion are given in Yang *et al.* (2016).

Figure 9 shows the time sequence of cross-sectional images captured at $x^* = 1.0$ for $C_m = 0.70\,\%$ and $f_e/f_0 = 0.5$ and 1.0. The imaging rate was 540 images per second such that four and eight images were obtained for each cycle of injection at $f_e/f_0 = 1.0$ and 0.5, respectively. The time intervals, $\Delta t = t_2 – t_1$, are 7.4 ms for $f_e/f_0 = 0.5$ (figure 9*a*) and 3.7 ms for $f_e/f_0 = 1.0$ (figure 9*b*), corresponding to one half of the

https://doi.org/10.1017/jfm.2018.376 Published online by Cambridge University Press

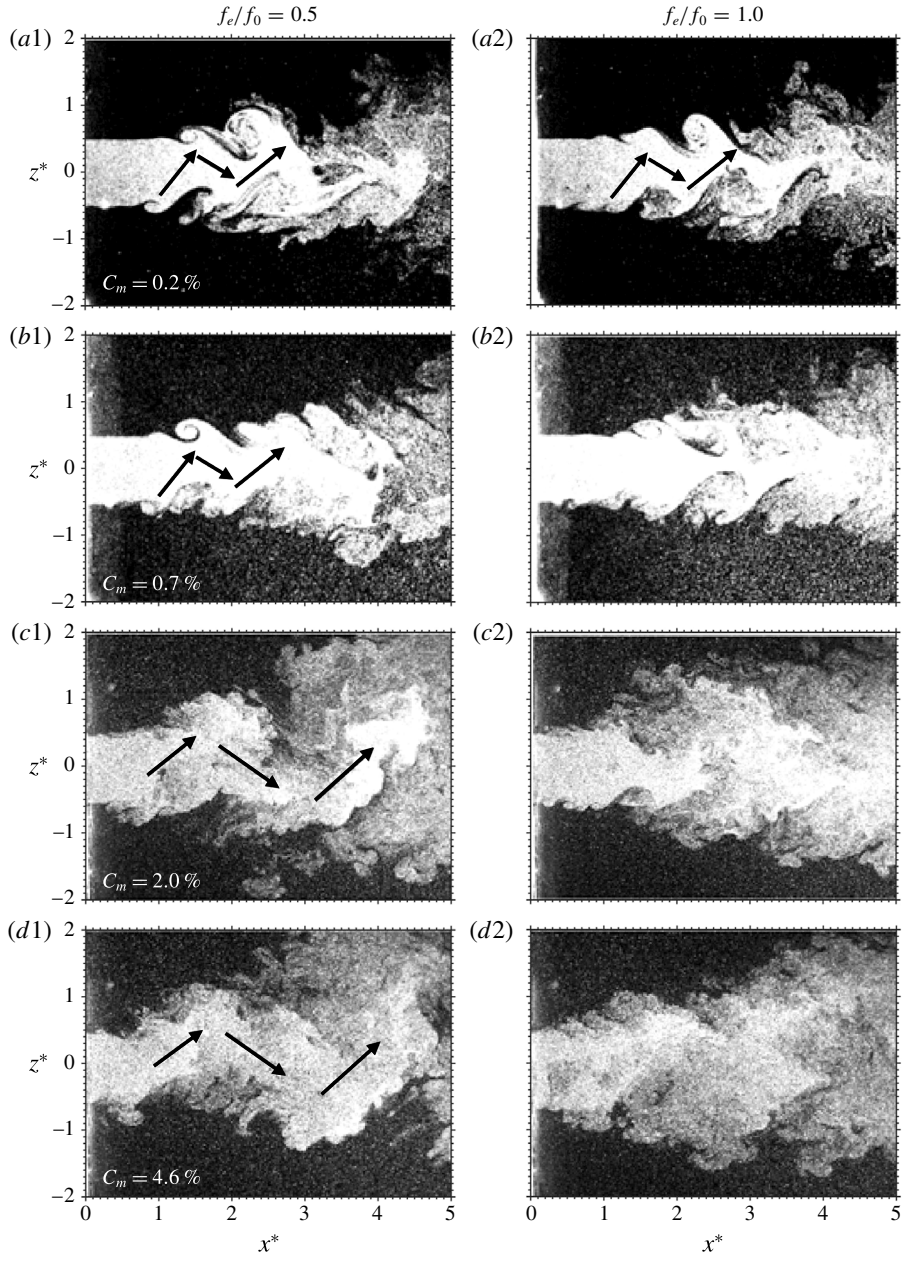


FIGURE 8. Typical flow structures in the injection plane of the jets from flow visualization ($\alpha = 0.1,\ d/D = 1/20$).

injection cycle for each case (the vortex shedding period is 7.4 ms). An incomplete ring structure is observed at $t_1 = 0$ on the minijet injection side ($z^* < 0$) for $f_e/f_0 = 0.5$ (figure 9*a*1), indicating the early roll up of vortical structures, but occurs largely on the other side ($z^* > 0$) at $t_2 \approx 7.4$ ms (figure 9*a*2). The difference in time between the captured incomplete ring structure of $z^* < 0$ and $z^* > 0$ is internally consistent with the flow structure development in the x–z plane (figure 8*b*1) where the lower shear layer

https://doi.org/10.1017/jfm.2018.376 Published online by Cambridge University Press

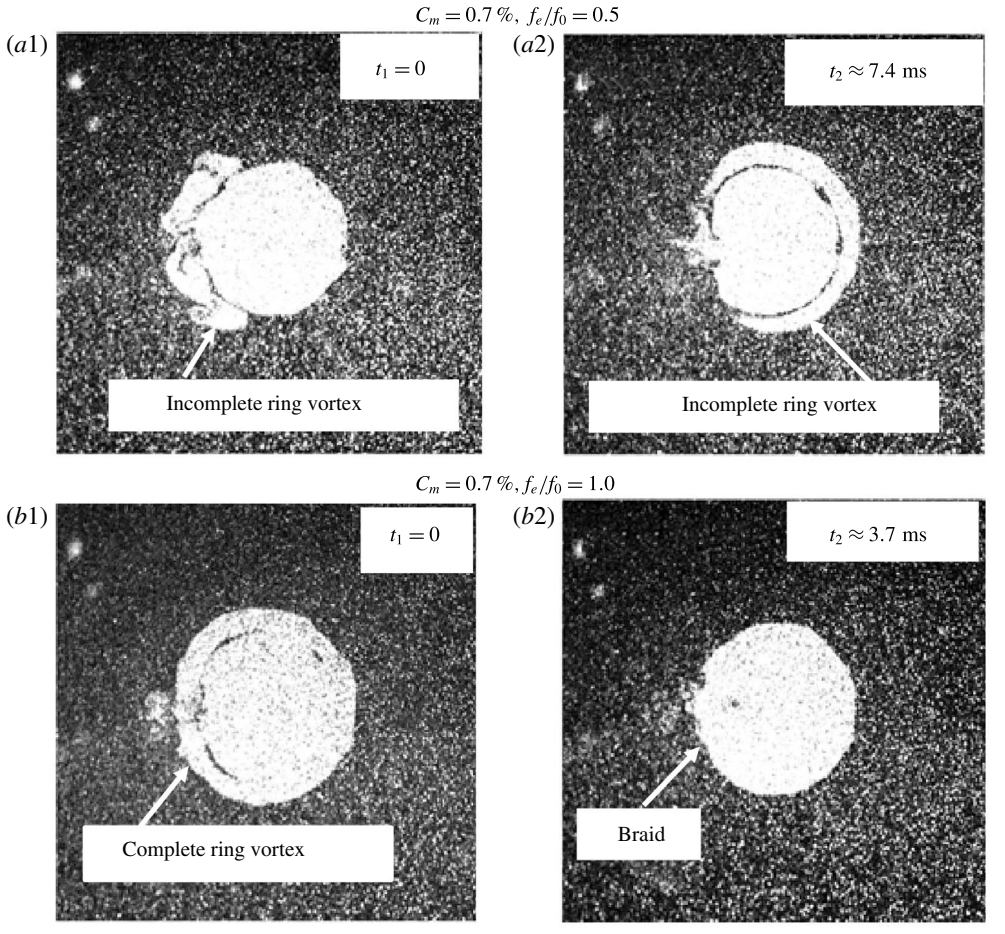


FIGURE 9. Typical flow structures of two sequential times in the cross-sectional planes of the perturbed jets at $x^* = 1.0$ from flow visualization ($C_m = 0.7\,\%$, $\alpha = 0.1$, $d/D = 1/20$).

($z^* < 0$) starts to roll up earlier than the upper ($z^* > 0$). It may be inferred that the part of the ring vortex on the minijet injection side forms early, compared with that on the other side. That is, the excitation at $f_e/f_0 = 0.5$ leads to the formation of inclined ring vortices, which evolve into the staggered arrangement (figure 8*b*1) and produce the main jet column flapping, as discussed by Yang *et al.* (2016). On the other hand, the images in figure 9(*b*1,*b*2) show a complete ring and a full-moon-like structure, albeit with breaches about the injection point, in the braid region, respectively, at $f_e/f_0 = 1.0$. That is, the ring vortices are not inclined and the jet column would not flap (figure 8*b*2). The assertion is further supported by the phase spectrum Φ_{U1U2} between U_1 and U_2 simultaneously measured at $z^* = -0.3$ and 0.3 ($x^* = 2$), respectively. At $f_e/f_0 = 0.5$, Φ_{U1U2} is near π or $-\pi$, i.e. anti-phased, displaying unmistakably a plateau about $f/f_e = 1.0$, regardless of C_m, (figure 10). The result indicates unambiguously that the flow structure shown in the left column of figure 8 is indeed representative of the flow. On the other hand, at $f_e/f_0 = 1.0$, Φ_{U1U2} is near zero at $f/f_e = 1.0$ for $C_m > 0.20\,\%$,

https://doi.org/10.1017/jfm.2018.376 Published online by Cambridge University Press

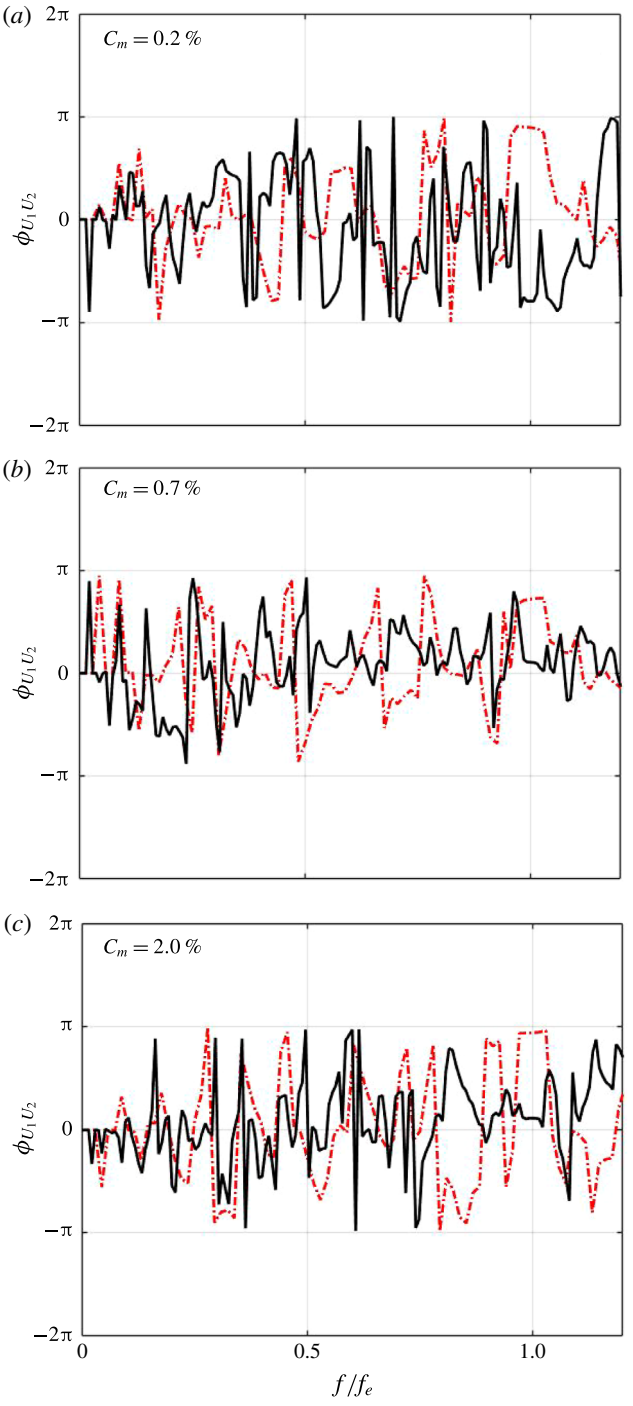


FIGURE 10. (Colour online) Spectral phase ϕ_{U1U2} between two streamwise velocity signals measured in the jet at $x^* = 2$ and $z^* = \pm 0.35$ excited at $\alpha = 0.1$ and $d/D = 1/20$. Dashed and continuous lines represent $f_e/f_0 = 0.5$ and 1.0, respectively.

https://doi.org/10.1017/jfm.2018.376 Published online by Cambridge University Press

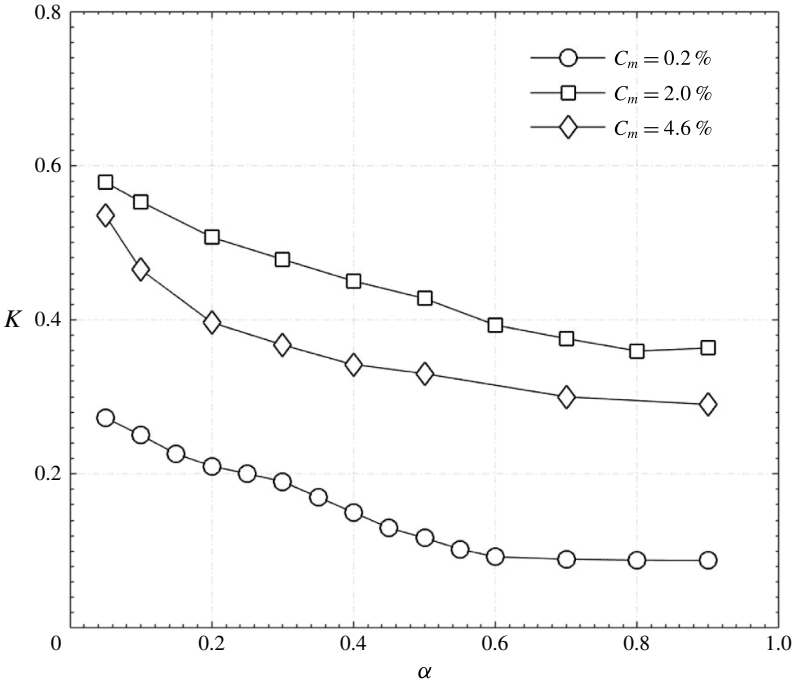


FIGURE 11. Dependence on α of the jet centreline mean velocity decay rate K ($f_e/f_0 = 0.5$, $d/D = 1/20$).

suggesting the absence of the flapping motion. It is the occurrence of flapping that increases significantly the jet decay rate or K, as shown in figure 7.

4.2. *Duty cycle effect*

The duty cycle α is the fraction of time the minijet is being injected during each injection cycle. This is a very important parameter for jet manipulation using unsteady minijet. However, there has been so far no report on the influence of α on the jet control performance. Figure 11 presents the dependence of K on α for three representative C_m at $f_e/f_0 = 0.5$. The K decreases from $\alpha = 0.1$ to 0.9 for all C_m, although varying little for $\alpha \geqslant 0.7$. At $\alpha = 0.1$ or 0.6, E_u measured at $(x^*, y^*, z^*) = (0.5, 0, -0.35)$ exhibits pronounced peaks at $f/f_e = 1.0$ ($f_e = 68$ Hz, $f_e^* = 0.23$) and its sub-harmonics (figure 12*a*,*b*) but not at $\alpha = 0.7$ (figure 12*c*), irrespective of C_m, suggesting that the natural preferred-mode instability is not excited at the larger α. Johari (2006) made a similar observation (see his figure 6) when studying the interaction of a pulsed jet in cross-flow at a large duty cycle, which they referred to as a quasi-steady blowing jet.

The duty cycle is connected to the penetration of the pulsed control jet (Johari *et al.* 1999). Consider the U signals at $\alpha = 0.1$ (figure 5), 0.5 and 0.9 (figure 13) along the z direction ($x^* = 0.05$, $C_m = 1.0\,\%$). At $\alpha = 0.1$, the periodic fluctuations of the signals, apparently originating from the minijet injection, appear from $z^* = -0.4$ to 0.4 and gradually increase in their magnitude as z^* increases. At $\alpha = 0.5$, the signals appear all fluctuating randomly, indicating a turbulent jet right from the nozzle exit. Note the gradual drop in the fluctuation magnitude from $z^* = 0.2$ to 0.4, distinctly different from that at $\alpha = 0.1$, suggesting a reduced penetration depth from $\alpha = 0.1$ to 0.5. This drop

https://doi.org/10.1017/jfm.2018.376 Published online by Cambridge University Press

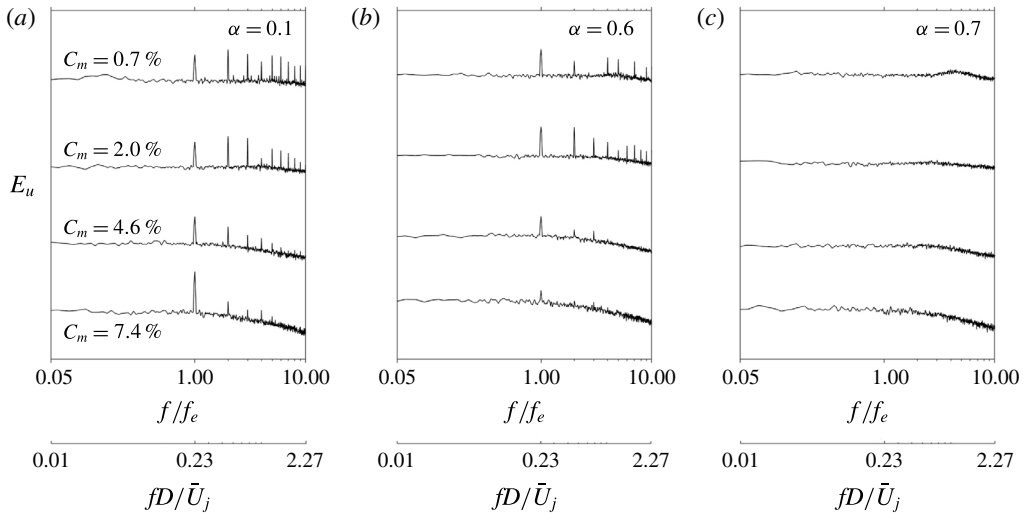


FIGURE 12. Power spectral density function of streamwise fluctuating velocity u measured at $x^* = 0.5$ and $z^* = -0.35$ for the jet excited at $f_e/f_0 = 0.5$ and $d/D = 1/20$.

is more obvious at $\alpha = 0.9$, where the velocity fluctuations are barely discernible at $z^* > 0.3$, that is, the penetration depth retreats further. It is worth pointing out that the decrease in the penetration depth with increasing α is due to the fact that, given the same C_m, the minijet injection velocity during the 'on-state' decreases with increasing α (figure 2*a*).

The change in the flow structure in the x–z plane (injection plane) under the influence of α is examined in figure 14 to seek the understanding of the flow physics behind the α effect on K (figure 11). As a reference, the unexcited jet is shown in figure 14(*a*). There is a profound change in the flow structure with and without excitation. In general, the shear layer rolls up early to form vortices in the injection plane (figure 14*b–f*). A large amount of ambient fluid (dark coloured) in the injection plane is entrained into the jet through the vortical structure, causing the jet to spread. The flow structure apparently flaps at $\alpha = 0.1$ (figure 14*b*) and the flow structure appears quite similar to each other from $\alpha = 0.3$ to 0.9 (figure 14*b–e*). Three successive vortices may be identified at $z^* \approx 0.5$ for $\alpha \geqslant 0.3$. The observations are consistent with the hot-wire signals. At $z^* = -0.4$ the signal exhibits sharp peaks for $\alpha = 0.1$ (figure 5), which are less sharped as α increases. The peaks originate from the minijet injection, which induces the early roll up of the ring structures. At $\alpha = 0.5$ and 0.9 the time interval between two successive peaks diminishes (figure 13). The ring vortices are clearly separated at $\alpha = 0.1$ and the increase in α leads to a reduced separation between the ring vortices.

We may gain an insight into the physics behind the ring vortex formation by examining the time sequence ($\Delta t \approx 3.7$ ms) of cross-sectional images captured at $x^* = 1.0$ for one cycle of injection (=1/68 s) for $\alpha = 0$ (unperturbed jet), 0.1, 0.5 and 0.9 ($C_m = 0.20\,\%$, figure 15). The unperturbed jet retains the circular shape of the nozzle exit (figure 15*a*1–*a*4), showing no roll-up motion. At t_1 and t_2 (figure 15*b*1–*b*2), an incomplete ring structure occurs in the region of $z^* < 0$ at $\alpha = 0.1$, indicating the early roll up of the vortex. But this structure cannot be captured for the next two images of the cycle (figure 15*b*3–*b*4). The observation suggests that at $\alpha = 0.1$ the

https://doi.org/10.1017/jfm.2018.376 Published online by Cambridge University Press

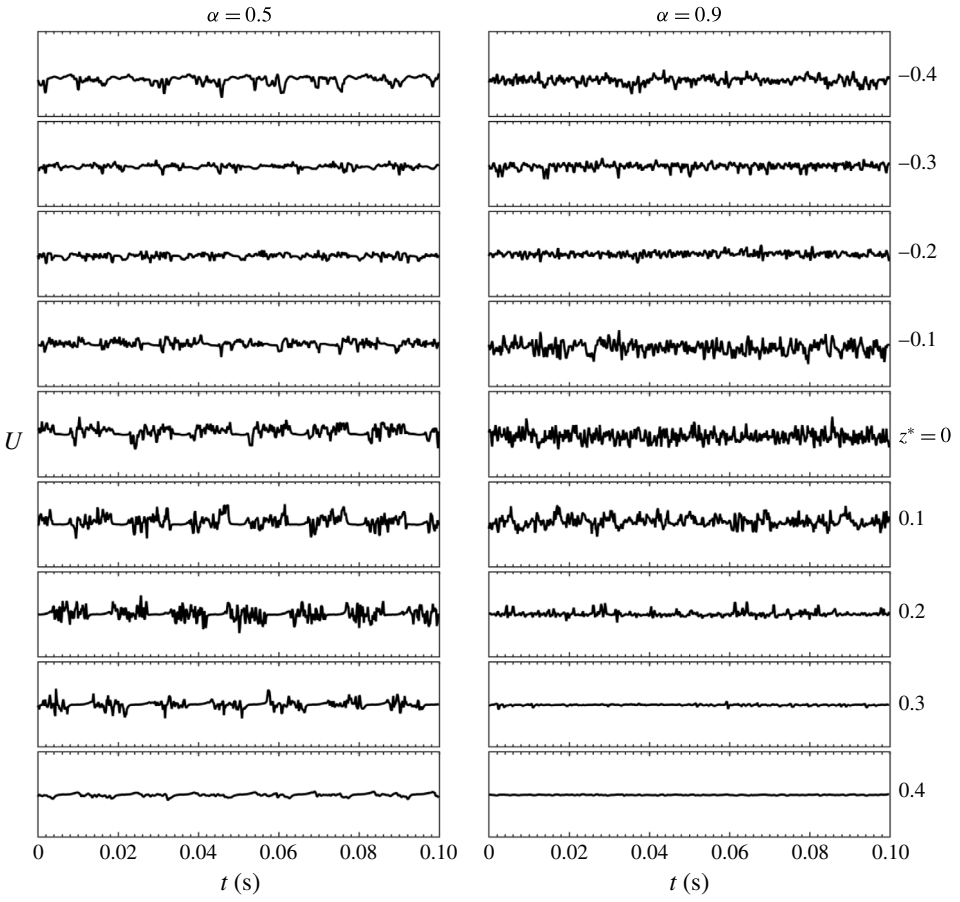


FIGURE 13. Typical signals of instantaneous streamwise U measured along the z^* direction in the plane of $x^* = 0.05$ ($C_m = 1.0\,\%$, $f_e/f_0 = 0.5$, $d/D = 1/20$). The same scale is applied for all signals.

vortex formed during one injection is clearly separated from that during next injection, as shown in figure 14(*b*). At $\alpha = 0.5$, an incomplete ring structure or a rupture on the circular jet column is captured for the first three images (figure 15*c*1–*c*3) and only disappears in the last image (figure 15*c*4). Clearly, an increase in α leads to a reduced gap between the successive injections, and the vortices in figure 14(*d*) appear to be closely separated, especially on the injection side. At $\alpha = 0.9$, the incomplete ring vortex is captured in figure 15(*d*1) and the rupture, progressively getting deeper, is evident for the next three images (figure 15*d*2–*d*4), suggesting a continuous penetration. In summary, the ring vortices are clearly separated at $\alpha = 0.1$ and an increase in α results in a reduced gap between perturbations at $\alpha = 0.5$ and even continuous perturbation and penetration at $\alpha = 0.9$.

Johari *et al.* (1999) and Eroglu & Breidenthal (2001) suggested that the duty cycle and excitation frequency of a control jet may influence the penetration, flow structure and mass mixing characteristics in a cross-flow. Hermanson, Wahba & Johari (1998) proposed that interaction between a jet and cross-flow is characterized by two parameters, i.e. the injection time $\tau = \alpha f_e$ and α. Short and long τ correspond to

https://doi.org/10.1017/jfm.2018.376 Published online by Cambridge University Press

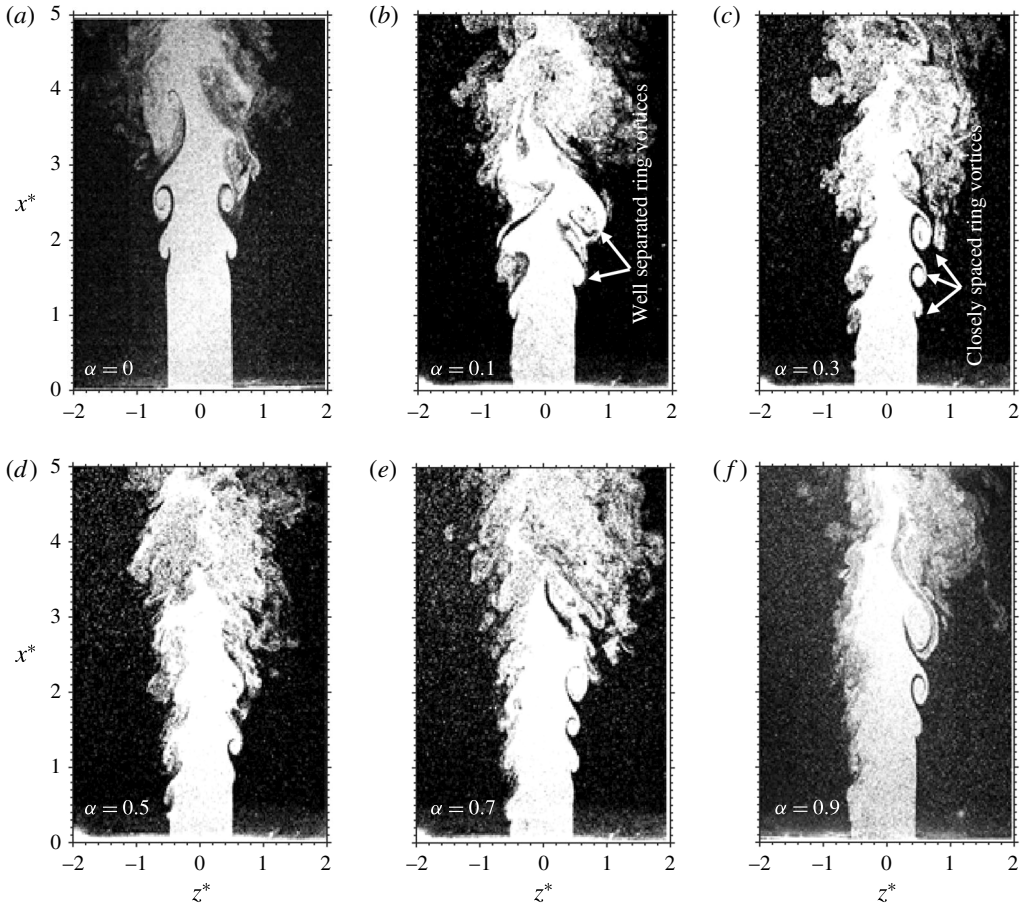


FIGURE 14. Typical flow structures in the injection and non-injection planes of the jet from flow visualization ($C_m = 0.2\,\%$, $f_e/f_0 = 0.5$, $d/D = 1/20$).

compact vortex rings and turbulent puff-like structures, respectively. On the other hand, the higher α leads to more intense interaction between turbulent jet puffs and correspondingly less jet penetration. In other words, the jet in cross-flow produces distinct vortex rings with spacing and strength dictated by f_e and α (Eroglu & Breidenthal 2001; Sau & Mahesh 2010; Coussement, Gicquel & Degrez 2012 and Karagozian 2014). For a given α, a higher f_e/f_0 reduces the time interval and hence spatial separation between two successive injections. Naturally, there should exist optimum α and f_e/f_0 in jet mixing enhancement. The present optimum α and f_e/f_0 to achieve the maximum K are 0.05 and 0.5, respectively (figures 7 and 11). Thus, under the optimal condition, the deep penetration and strong well-separated vortices are produced, leading to the flapping motion and hence mixing enhancement. At higher α, the vortex rings excited by the successive pulses interact among themselves, thereby adversely affecting the mixing capability.

4.3. *Mass flow rate ratio effect*

The decay rate K exhibits a strong dependence on C_m (figure 16), which can be divided into two categories based on the mechanisms. In Category I ($C_m < 4.6\,\%$), K is

https://doi.org/10.1017/jfm.2018.376 Published online by Cambridge University Press

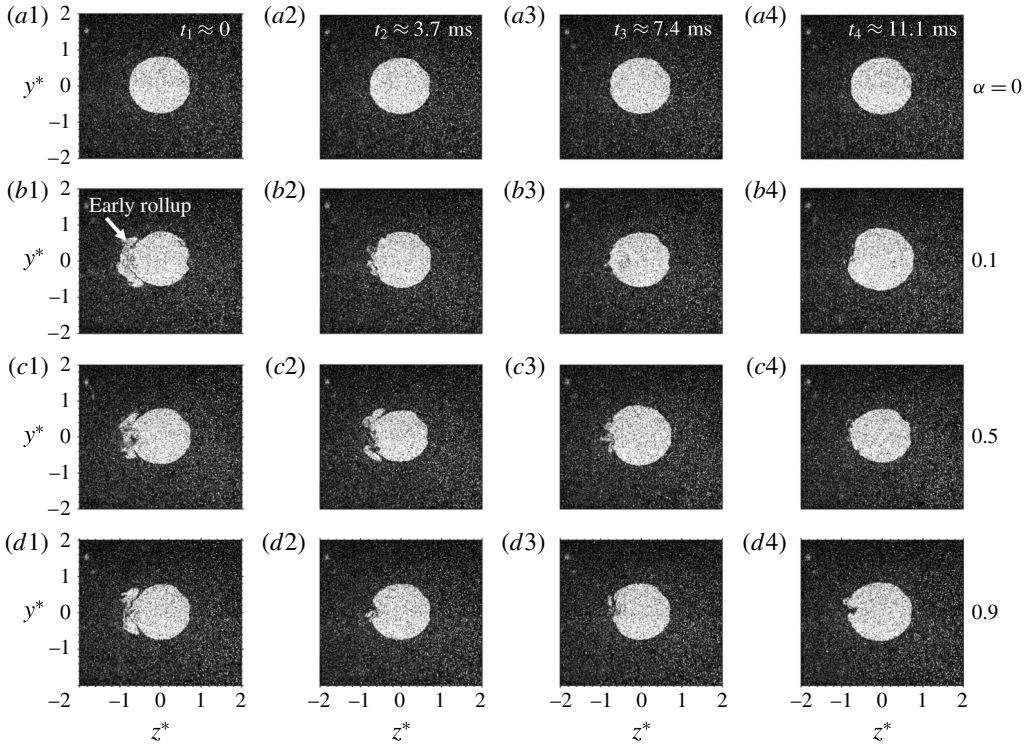


FIGURE 15. Time sequence ($\Delta t \approx 0.03$ ms) of the flow structure in the y–z plane ($x^* = 1.0$) of the jet from flow visualization ($C_m = 0.2\,\%$, $f_e/f_0 = 0.5$, $d/D = 1/20$).

highly sensitive to C_m, rising rapidly from 0.16 at $C_m = 0.04\,\%$ to approximately 0.56 at $C_m = 2.0\,\%$ and then dropping quickly until $C_m = 4.6\,\%$. The enhanced K results largely from the greatly modified organized motions or the generation of the flapping jet column. The maximum K of Category I reaches 0.56, approximately 19 times that (0.03) of the natural jet and over 1.6 times that (0.34) under steady minijet injection given the same C_m (= 2.0 %). This maximum occurs at the maximum penetration depth (figure 5). The drop in K from $C_m = 2.0\,\%$ until 4.6 % is a result of reduced flapping strength due to the adverse effect of turbulence generation on the organized structure development. The flapping jet is characterized by $\Phi_{U1U2} = \pi$ (Yang *et al.* 2016), which is found to decrease from π at $C_m = 2.0\,\%$ (figure 10*c*) to 0.3 at $C_m =$ 4.6 % (not shown). In Category II ($C_m \geqslant 4.6\,\%$), the jet column flapping disappears; however, K increases steadily, albeit much less rapidly than in Category I, and appears approaching asymptotically to a constant. The increase in K is essentially due to the enhanced turbulence with increasing C_m (Yang & Zhou 2016). In summary, it is a difference in the vortex dynamics that produces a great variation in K.

It is worth examining the dependence on C_m of the potential core length L^*_{PC}, over which $\bar{U}^*$ on the centreline is constant, for Categories I and II. This length is an authentic measure to quantify mixing. Shorter this length higher is the mixing enhancement due to the control (e.g. Bradbury & Khadem 1975). Figure 17(*a*) presents the variation of $\bar{U}^*$ along the jet centreline for various C_m. In Category I, L^*_{PC} is 2.5, 1.0 and 0 for $C_m = 0.5\,\%$, 1.0 % and 2.0 %, respectively, that is, L^*_{PC} contracts for increasing C_m. $L^*_{PC} = 0$ at $C_m = 2.0\,\%$ points to rapid mixing (figure 8*c*1)

https://doi.org/10.1017/jfm.2018.376 Published online by Cambridge University Press

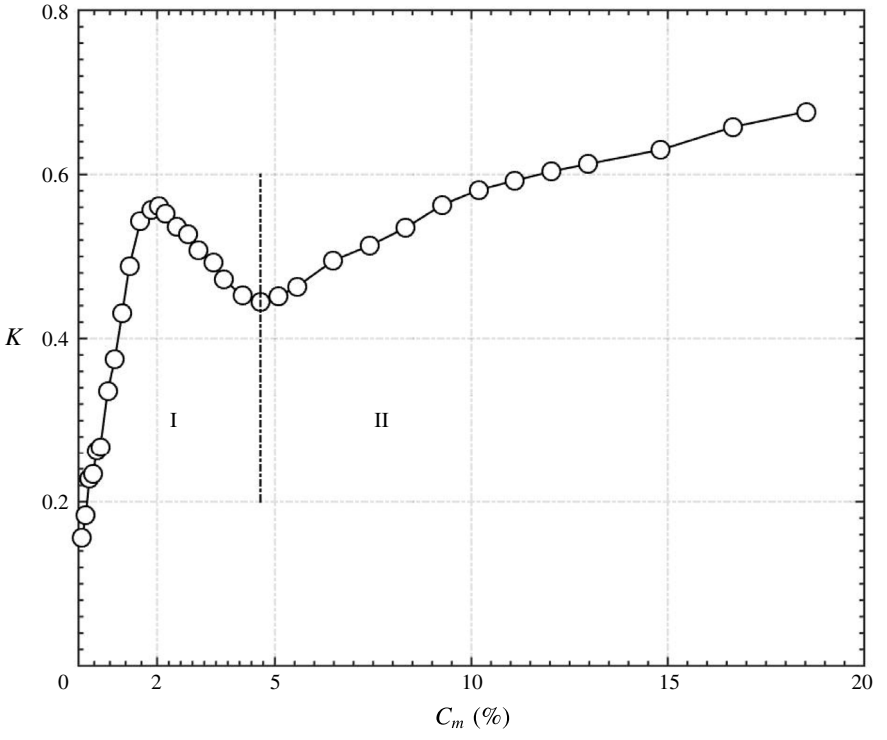


FIGURE 16. Dependence on C_m of the jet centreline mean velocity decay rate K ($f_e/f_0 = 0.5,\ \alpha = 0.1,\ d/D = 1/20$).

right from the nozzle exit, corresponding to the local maximum peak in K (figure 16). With further increase in C_m, L^*_{PC} remains at zero (figure 17*a*) but the turbulence level rises continuously, which is responsible for the steady drop in $\bar{U}^*$ and a great enhancement in u^*_{rms} over $0 < x^* < 3$ (figure 17*b*). However, the decay of $\bar{U}^*$ is approximately linear over $3 < x^* < 6$, along with a continuous drop in u^*_{rms}. The combined effect leads to a decrease in K from $C_m = 2.0\,\%$ to $4.6\,\%$.

4.4. *Diameter ratio effect*

The K exhibits a strong dependence on d/D (figure 18). A number of observations can be made. Firstly, for all d/D the dependence of K on C_m ($f_e/f_0 = 0.5$ and $\alpha = 0.1$) is qualitatively the same and may be divided into two categories, i.e. a rapid rise to a local maximum K followed by a drop (Category I) and then a monotonic growth with increasing C_m (Category II). Secondly, for a given small C_m ($<1\,\%$) in Category I, the decay rate for $d/D = 1/40$ is in general significantly larger than that for $d/D = 1/25$, and the latter exceeds that for $d/D = 1/20$, that is, the smaller d/D is more efficient in enhancing mixing than the larger. This is because at a given C_m the smaller d/D is associated with a larger penetration depth due to the increased injection velocity. However, this trend may be reversed at C_m exceeding $1\,\%$. Once the penetration depth reaches the maximum, a further increase in C_m will enhance the impingement strength upon the wall, thus producing turbulence and adversely influencing the development of the organized motions or jet flapping. As a consequence, K contracts. Thirdly, the monotonic growth in K with increasing C_m in

https://doi.org/10.1017/jfm.2018.376 Published online by Cambridge University Press

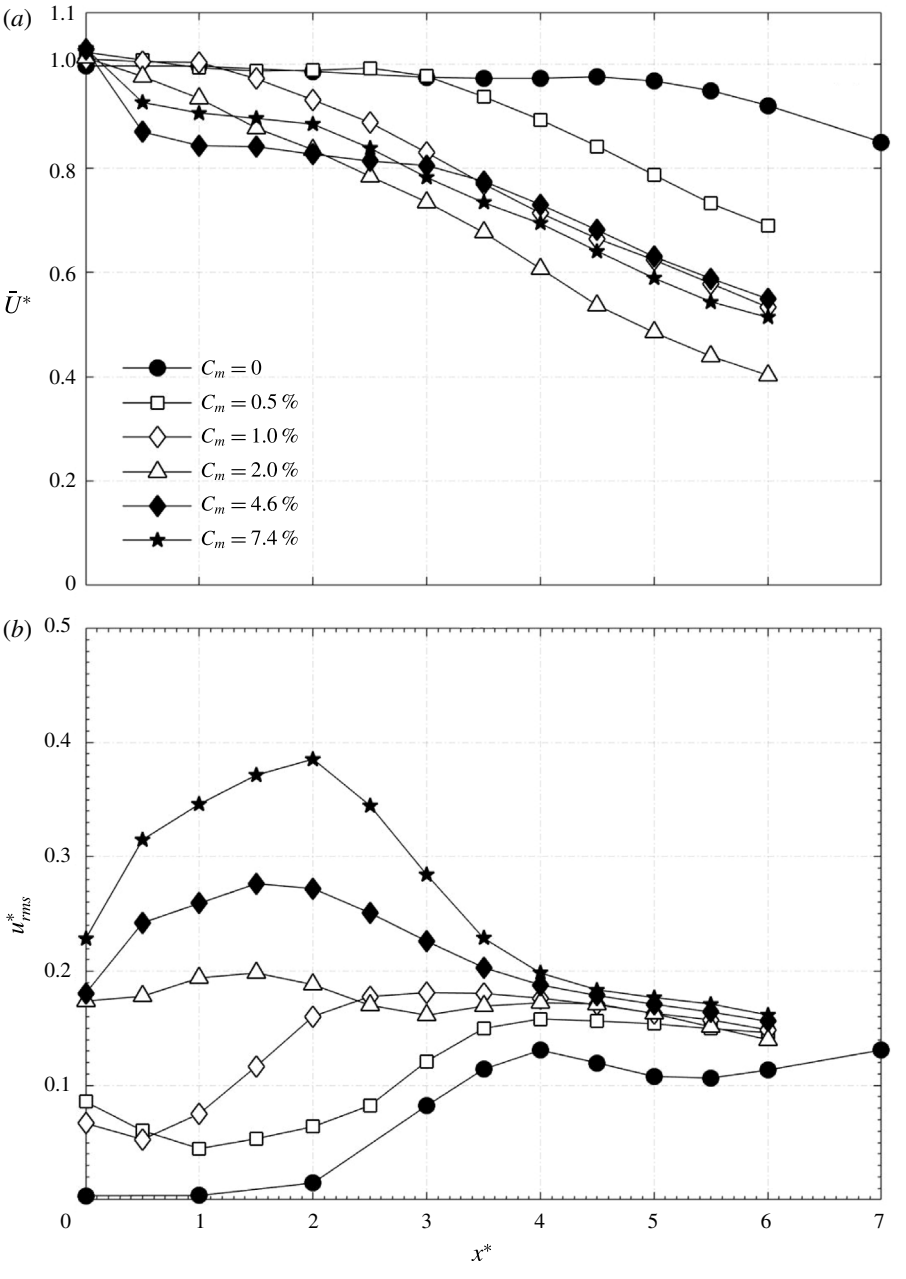


FIGURE 17. (*a*) Streamwise mean velocity $\bar{U}^*$ and (*b*) root mean square velocity u^*_{rms} along the jet centreline ($f_e/f_0 = 0.5$, $\alpha = 0.1$, $d/D = 1/20$) for various C_m in Category I.

Category II is approximately linear, irrespective of d/D, with almost the same slope. Finally, the K for different d/D reaches the local maximum at a different C_m or the momentum in Category I. The larger d/D corresponds to a greater C_m and also a greater local maximum K. While the maximum penetration depth might be the same for different d/D, the corresponding momentum is higher, as a result of bigger C_m,

https://doi.org/10.1017/jfm.2018.376 Published online by Cambridge University Press

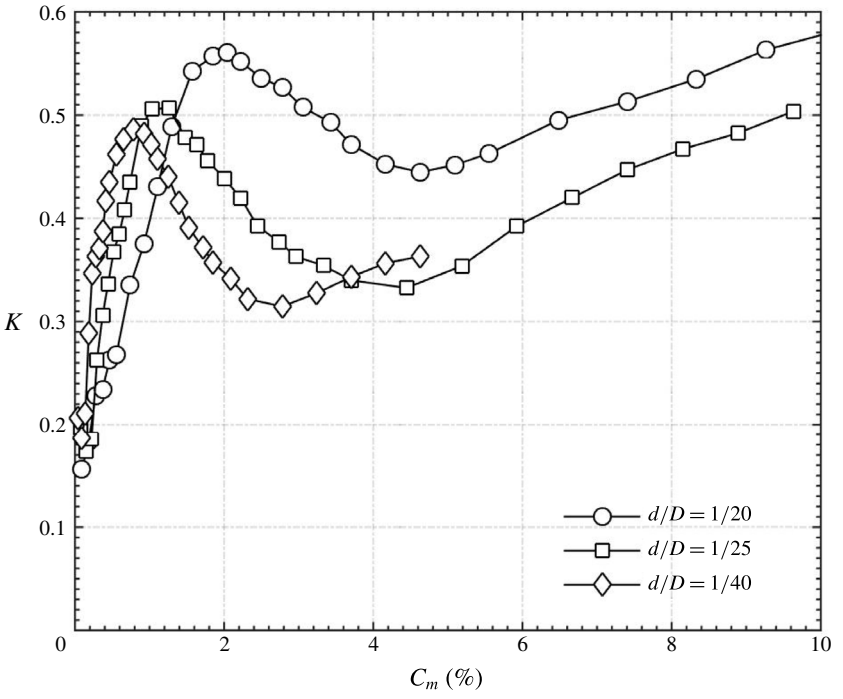


FIGURE 18. Dependence on d/D on the jet centreline mean velocity decay rate K ($f_e/f_0 = 0.5,\ \alpha = 0.1$).

for the larger d/D. This higher momentum should promote to a greater extent the strength of the large-scale vortices and hence the strength of jet column flapping. Consequently, the corresponding local maximum K is larger.

5. Empirical scaling of jet decay rate

As shown in § 4, K depends on C_m, f_e/f_0, α and d/D, i.e. $K = g_1\ (C_m, f_e/f_0, \alpha, d/D)$. In this paper, g_i is a function, where $i = 1, 2, 3, 4$. An empirical scaling analysis is performed for the jet decay rate in order to find a scaling factor ξ so that $K = g_1\ (C_m, f_e/f_0, \alpha, d/D)$ may be reduced to $K = g_2\ (\xi)$. Valuable insight into the flow control physics behind the influence of the minijet parameters on the flow development may be gained out of this analysis. Scaling analysis also provides the information of the control parameters on extending the laboratory experiments to the full-scale application, i.e. guiding the flow control in practical applications.

As is clear in figure 18, the dependence of K on C_m ($f_e/f_0 = 0.5$ and $\alpha = 0.1$) remains unchanged qualitatively as d/D varies. Given the same C_m, the minijet velocity increases as d/D is reduced. Physically, the penetration depth of the minijet is determined by the combined effect of the minijet mass flow rate and the minijet exit velocity, that is, the momentum of the minijet plays an important role in determining the overall effectiveness in jet manipulation. After careful physical analysis of the experimental data in figure 18 along with many trial-and-error attempts, it has been found that the rescaled K or $K(D/d)^{0.25}$ collapses reasonably well in Category I for various d/D (figure 19*a*) provided that the abscissa is given in terms of the momentum ratio $MR = \dot{m}_m \bar{U}_m / \dot{m}_j \bar{U}_j$ of the minijet to main jet, where $\dot{m}$ and $\bar{U}$ represent the jet

https://doi.org/10.1017/jfm.2018.376 Published online by Cambridge University Press

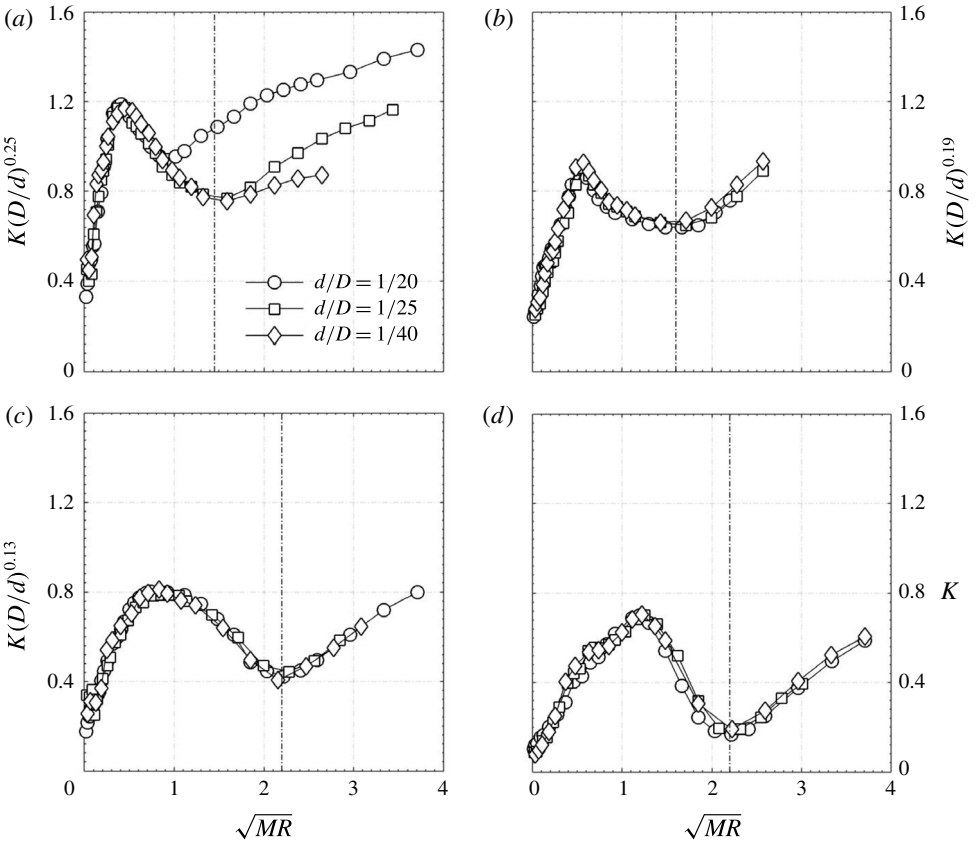


FIGURE 19. Dependence of the re-scaled centreline mean velocity jet decay rate on $\sqrt{MR}$ ($f_e/f_0 = 0.5$, $\alpha = 0.1$); (*a*) $\alpha = 0.1$, (*b*) 0.3, (*c*) 0.5, (*d*) 0.9.

mass flow rate and exit velocity, respectively, and subscripts m and j denote minijet and main jet, respectively. MR can be further written as $= (\dot{m}_m/\dot{m}_j)^2(\rho_j/\rho_m)(A_j/A_m)$, where ρ and A are the density of fluid (air) and the exit area of the minijet or nozzle exit, respectively. For incompressible flow, $MR = (\dot{m}_m/\dot{m}_j)^2(D/d)^2 = C_m^2(D/d)^2$. One may question whether the incompressible assumption is valid for the minijet injection at large C_m. Given $C_m < 8.2\,\%$, the error incurred in estimating the minijet velocity from the incompressible assumption is no more than 3 %. Please refer to the Appendix for the determination of errors. The result indicates that $\sqrt{MR}$ is the controlling scaling factor. The dependence of $K(D/d)^{0.25}$ on $\sqrt{MR}$ for $d/D = 1/20$ does not collapse for $\sqrt{MR} > 1.0$ with those for $d/D = 1/25$ and $1/40$. This is because the injected flow through the minijet nozzle of very small diameter ($d/D \leqslant 1/25$) may have been partially choked at a large C_m, thus resulting in a K value smaller than that expected.

A similar collapse is obtained for $\alpha = 0.3$, 0.5 and 0.9 (figure 19*b–d*), although the measured K is now re-scaled to $K(D/d)^{0.19}$, $K(D/d)^{0.13}$ and $K(D/d)^{0.00}$, respectively. As a matter of fact, this collapse is well observed for Category II as well as Category I since the choking phenomenon may not occur for $\alpha \geqslant 0.3$ in the present experimental conditions. Apparently, the power index n depends on α, which are interestingly linearly correlated by $n = C\alpha + 0.28$ for $\alpha = 0.1 - 0.9$, where C is -0.31 (figure 20).

https://doi.org/10.1017/jfm.2018.376 Published online by Cambridge University Press

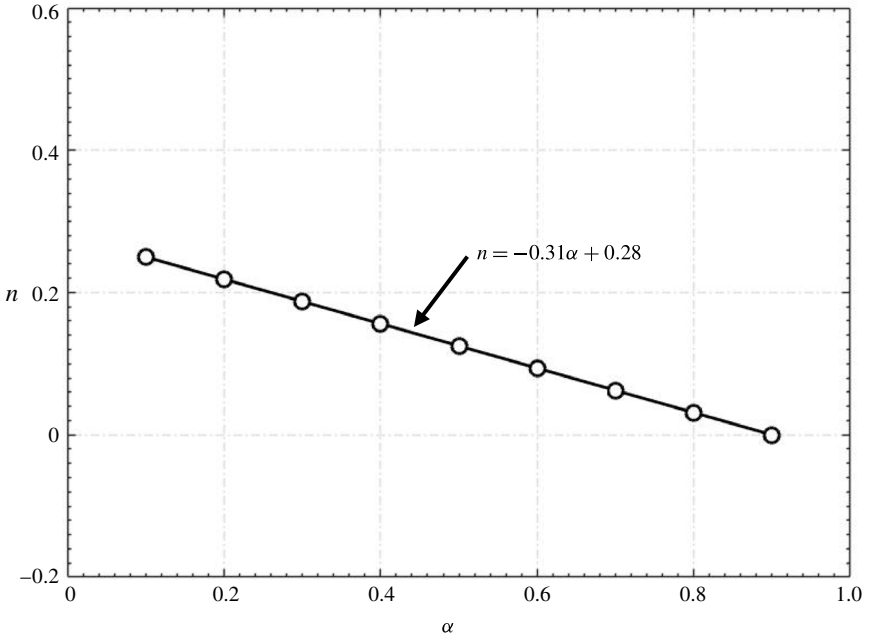


FIGURE 20. Variation of n in $K(D/d)^n$ with α.

As such, we may write $K(D/d)^n = g_3\ (\sqrt{MR})$, where $n = -0.31\alpha + 0.28$. Note that $n < 0.06$ for $\alpha > 0.7$, that is, n is approximately zero, as shown in figure 20, and the corresponding minijet injection may be referred to as the quasi-steady injection.

In figures 19 and 20, f_e/f_0 is fixed at 0.5. One may wonder whether the rescaled K or $K(D/d)^n$ would collapse over the range of f_e/f_0 examined. Figure 21 illustrates at $\alpha = 0.1$ and 0.3 that $K(D/d)^n$ collapses for different d/D, that is, n is independent of f_e/f_0. We will discuss in detail the physical meaning of $(D/d)^n$ later in this section.

A careful analysis along with numerous trial-and-error attempts at least-squares fitting of the data in Category I indicates that the relationship between $K(D/d)^n$, $\sqrt{MR}$ and α may be written as

$$K\left(\frac{D}{d}\right)^n = g_4\left(\frac{\sqrt{MR}}{\alpha}\right), \tag{5.1}$$

where $\sqrt{MR}/\alpha = (C_m/\alpha)(D/d)$ is physically the momentum per pulse of injection. Apparently, for a given minijet diameter and C_m, an increase in α results in a reduced momentum per pulse of injection and subsequently a reduced penetration depth into the main jet. Consequently, K decreases, as illustrated in figure 11. On the other hand, for given C_m and α, a decrease in the minijet diameter results in increased $\sqrt{MR}/\alpha$ or penetration depth and hence a higher K provided that the choking phenomenon is absent.

In order to determine g_4, we plot $K(D/d)^n$ against $\sqrt{MR}/\alpha$ (not shown), which displays a collapse of the data and is approximately piecewise linear, albeit branched. Therefore, the data are replotted in figure 22 showing the dependence of K on $(\sqrt{MR}/\alpha)(d/D)^n$. All the data are from Category I or the left-hand side of the

https://doi.org/10.1017/jfm.2018.376 Published online by Cambridge University Press

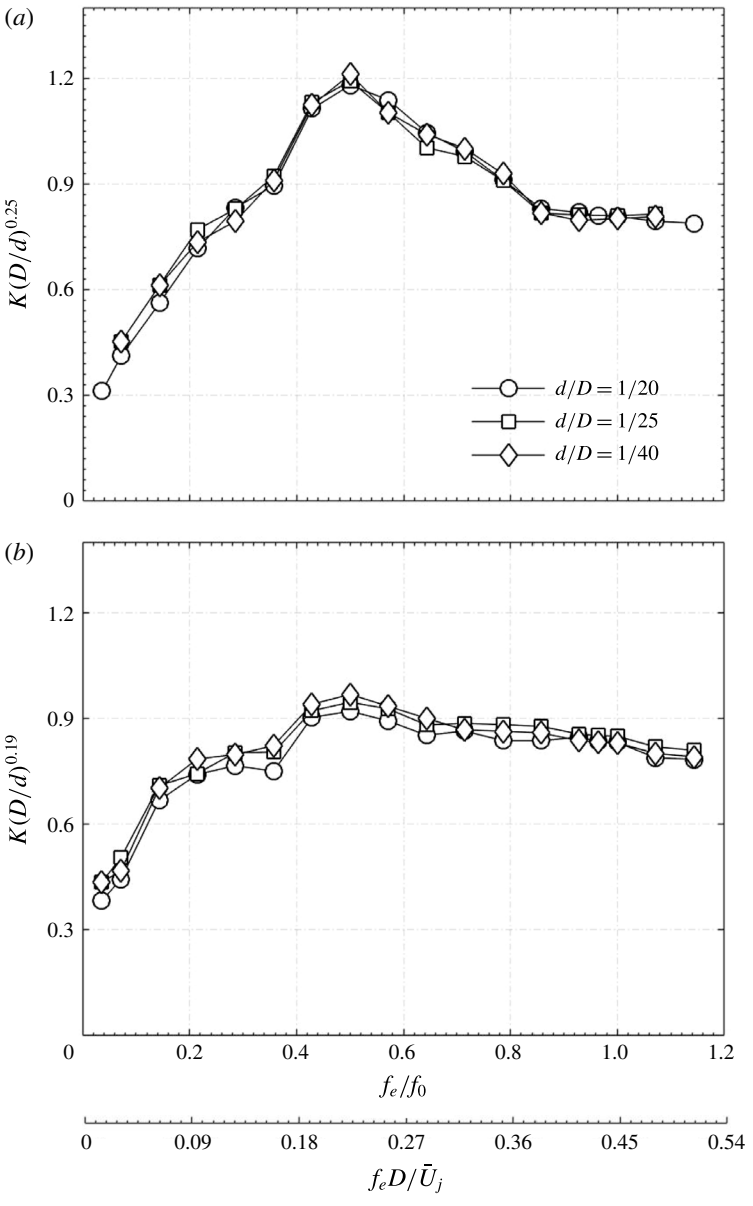


FIGURE 21. Dependence on f_e/f_0 or $f_eD/\bar{U}_j$ of the rescaled centreline mean velocity jet decay rate. (*a*) $\sqrt{MR} = 0.4$, $\alpha = 0.1$; (*b*) $\sqrt{MR} = 0.5$, $\alpha = 0.3$.

vertical broken line in figure 19, with the additional data of $\alpha = 0.7$. The data of K display a quite good collapse up to $\xi \equiv (\sqrt{MR}/\alpha)(d/D)^n \approx 1.0$ but branch into four, i.e. $B1$, $B2$, $B3$ and $B12$ for $\xi > 1.0$. The data are piecewise least-squares fitted to linear curves, *viz.*

$$K = 0.42\xi + 0.14 \quad \text{for } 0 \leqslant \xi \leqslant 1.0\text{–}1.5 \text{ (depending on } \alpha \text{ and } d/D), \tag{5.2a}$$

$$B1\text{:} \quad K = -0.45\xi + 1.37 \quad \text{for } \xi > 1.5, \tag{5.2b}$$

https://doi.org/10.1017/jfm.2018.376 Published online by Cambridge University Press

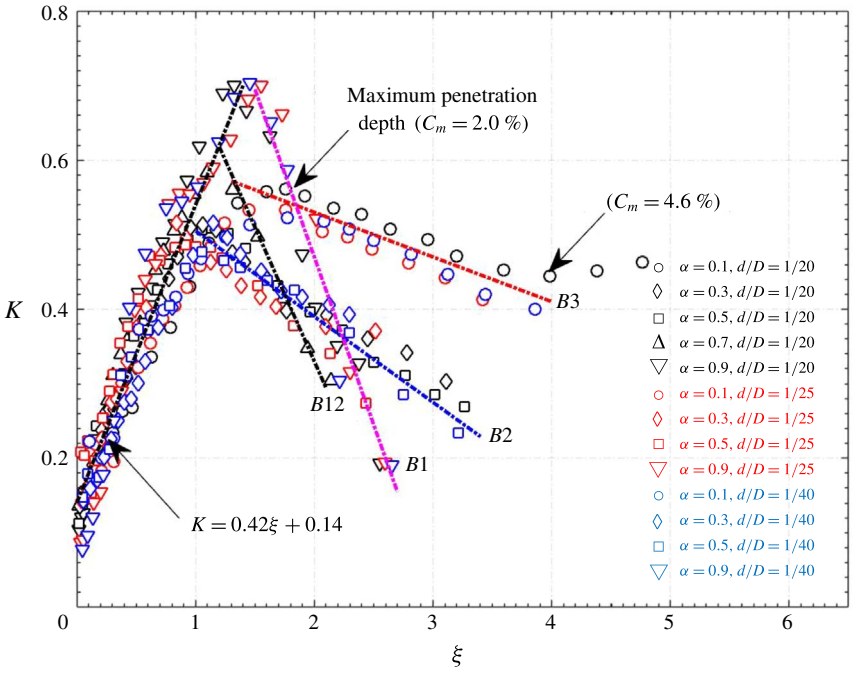


FIGURE 22. (Colour online) Dependence of the centreline mean velocity jet decay rate K on $\xi = (\sqrt{MR}/\alpha)(d/D)^n$ where $n = 0.25$–0. All the data are from the left-hand side of the local peak line in figure 19.

$$B2: \quad K = -0.12\xi + 0.65 \quad \text{for } \xi > 1.0, \tag{5.2c}$$

$$B3: \quad K = -0.07\xi + 0.62 \quad \text{for } \xi > 1.0, \tag{5.2d}$$

$$B12: \quad K = -0.36\xi + 1.05 \quad \text{for } \xi > 1.0. \tag{5.2e}$$

The measured K may deviate from the calculation from (5.2) by no more than 10 %, with a 95 % confidence; the only exception is $\xi < 0.2$ where the deviation may go up to $\pm 15\,\%$.

Before discussing the results in figure 22, we need to understand physically $(d/D)^n$. Take the case of $d/D = 1/20$ and $1/40$ for example. As d/D is reduced from $1/20$ to $1/40$, C_m required to achieve a predefined K, say 0.3, should be less based on figure 18. We define a percentage reduction by

$$\Delta C_{m_{d/D}} = 1 - \frac{[C_m]_{1/40}}{[C_m]_{1/20}}, \tag{5.3}$$

where subscripts $1/40$ and $1/20$ denote diameter ratios (d/D). The required C_m for given K, α and d/D can be calculated from (5.2*a*):

$$K \approx \frac{\sqrt{MR}}{\alpha}\left(\frac{d}{D}\right)^n \approx \frac{C_m}{\alpha}\left(\frac{D}{d}\right)^{1-n}, \tag{5.4}$$

or

$$C_m \approx K\alpha\left(\frac{d}{D}\right)^{1-n}. \tag{5.5}$$

https://doi.org/10.1017/jfm.2018.376 Published online by Cambridge University Press

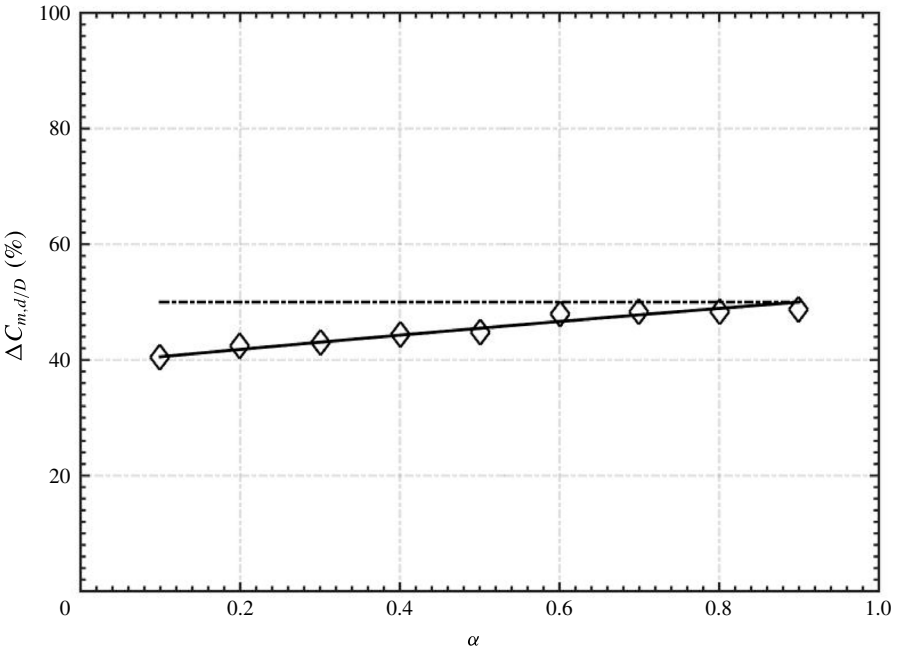


FIGURE 23. Variation in $\Delta C_{m,d/D}$ with α as d/D changes from 1/20 to 1/40.

Then $\Delta C_{m_{d/D}}$ can be obtained by substituting (5.5) into (5.3) for the corresponding d/D. The variation in $\Delta C_{m_{d/D}}$ with α is shown in figure 23. A decrease in d/D by half results in a drop in the required C_m by approximately half ($\Delta C_{m_{d/D}} \approx 50\,\%$) for $\alpha \geqslant 0.7$. $\Delta C_{m_{d/D}}$ contracts to 0.4 or 40 % for $\alpha = 0.1$. The fact that additional C_m, proportional to $(d/D)^{-n}$ (5.5), is required to achieve a given K due to a reduced d/D is physically due to the increased retardation effect of the minijet orifice. A reduction in α further amplifies this retardation effect. That is, $(d/D)^{-n}$ reflects physically the retardation effect in case of small d/D or α.

The scaling factor $\xi = (\sqrt{MR}/\alpha)(d/D)^n$ is physically the effective momentum ratio per pulse of the minijet and determines the level of K. On the other hand, the penetration depth of the control jet into the main jet also determines the level of mixing (Johari *et al.* 1999; Johari 2006). One question arises: are the two parameters connected? Yang (2017) demonstrated that the penetration depth and the distribution of u^*_{rms} measured at the exit of the main jet are closely correlated. Figure 24 compares the u^*_{rms} distributions across the jet, measured at $x^* = 0.05$, corresponding to $\xi \approx 0.40$, 0.90 and 2.0. It is evident that, given the same ξ, the u^*_{rms} distributions are qualitatively the same despite different combinations of α and C_m. The observation suggests that the penetration depth is the same for the same ξ, thus implying a correspondence between ξ and the penetration depth. Furthermore, the flow structure and its downstream development are essentially the same for the same ξ. As illustrated in figure 25, the flow structures captured at $\xi \approx 0.40$ in the injection and non-injection planes are qualitatively the same, including the starting roll-up position and the topological arrangement of vortices, in spite of the three different combinations of C_m and d/D. In fact, the corresponding jet mean velocity half-width $z^*_{0.5}$ (e.g. Ball, Fellouah & Pollard 2012), measured using PIV, in the injection plane of the perturbed jet displays a good collapse over $x^* \approx 0$–5 (figure 26).

https://doi.org/10.1017/jfm.2018.376 Published online by Cambridge University Press

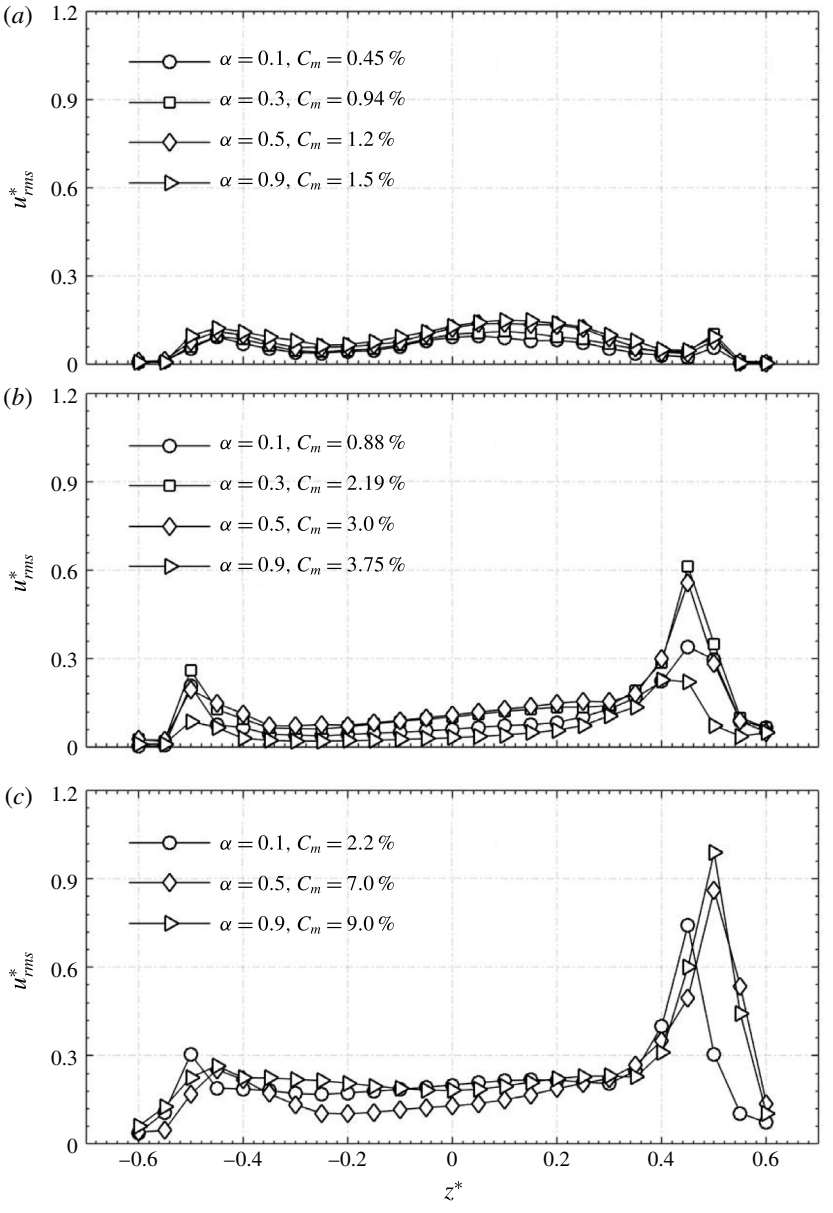


FIGURE 24. Radial distributions of turbulent intensity $u^*_{rms} = u_{rms}/\bar{U}_j$ measured at $x^* = 0.05$ ($f_e/f_0 = 0.5$, $d/D = 1/20$). (*a*) $\xi \approx 0.40 \pm 0.06$; (*b*) 0.90 ± 0.06; (*c*) 2.0 ± 0.06.

Now let us turn to the discussion of the results presented in figure 22. For $\xi \leqslant 1.0$, K rises rapidly and almost linearly with increasing effective momentum ratio per pulse of the minijet, as expected. As an interesting comparison, Edwards, Sherman & Breidenthal (1985) and Breidenthal *et al.* (1985) found that the decay rate of the fluctuating concentration c_{rms} was linearly connected to the momentum ratio of the transverse jet to the rectangular duct flow. Beyond $\xi = 1.0$, K may follow four distinct branches. The large deviation in K between the branches is physically connected to

https://doi.org/10.1017/jfm.2018.376 Published online by Cambridge University Press

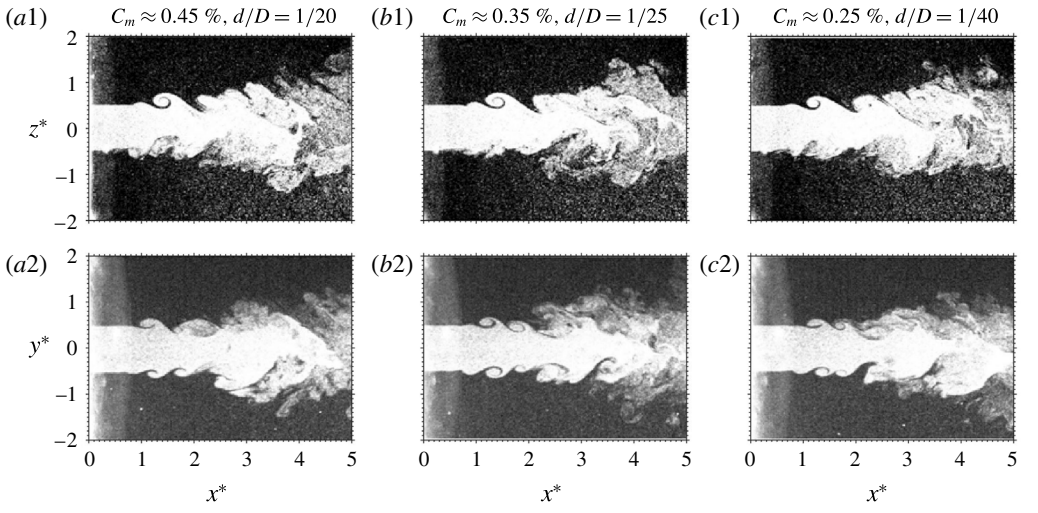


FIGURE 25. Typical flow visualization photographs captured in the injection and non-injection planes of the jet ($\alpha = 0.1$, $f_e/f_0 = 0.5$) given $K = 0.3$ and the same $(\sqrt{MR}/\alpha)(d/D)^n \approx 0.40 \pm 0.06$.

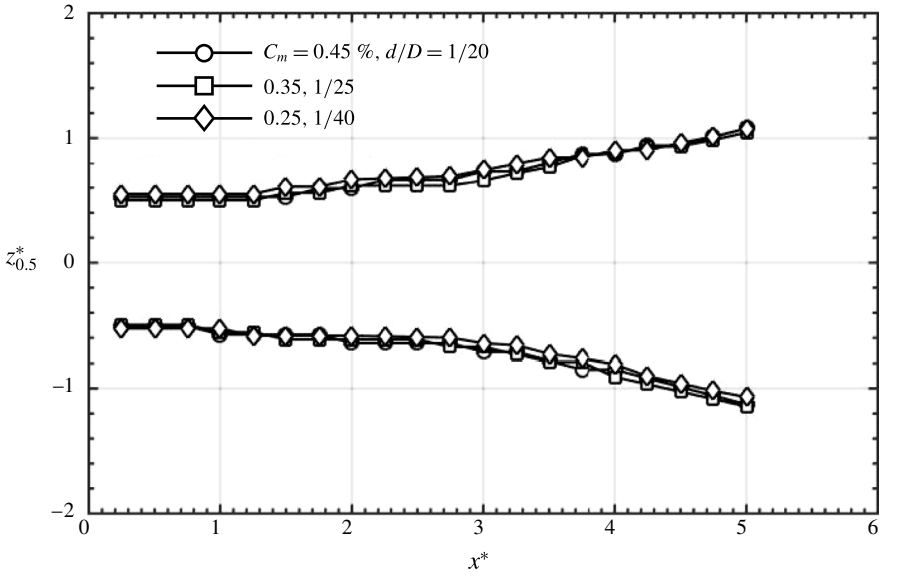


FIGURE 26. Downstream variation in the jet mean velocity half-width $z^*_{0.5}$ ($\alpha = 0.1$, $f_e/f_0 = 0.5$) given $K = 0.3$ and the same $(\sqrt{MR}/\alpha)(d/D)^n \approx 0.40 \pm 0.06$: $d/D = 1/20$.

the retardation experienced at large ξ (> 1.0) and the jet column deflection. A close look at the data in this figure unveils that the four branches are associated with distinct α. The maximum K of $B1$ exceeds considerably that of $B12$, $B3$ or $B2$. To understand this difference, the typical flow visualization images corresponding to the maximum K of each branch are compared between the four cases. The maximum K, 0.56, of $B3$ occurs at $\xi \approx 1.8$ ($C_m = 2.0\,\%$ and $d/D = 1/20$), corresponding to the

https://doi.org/10.1017/jfm.2018.376 Published online by Cambridge University Press

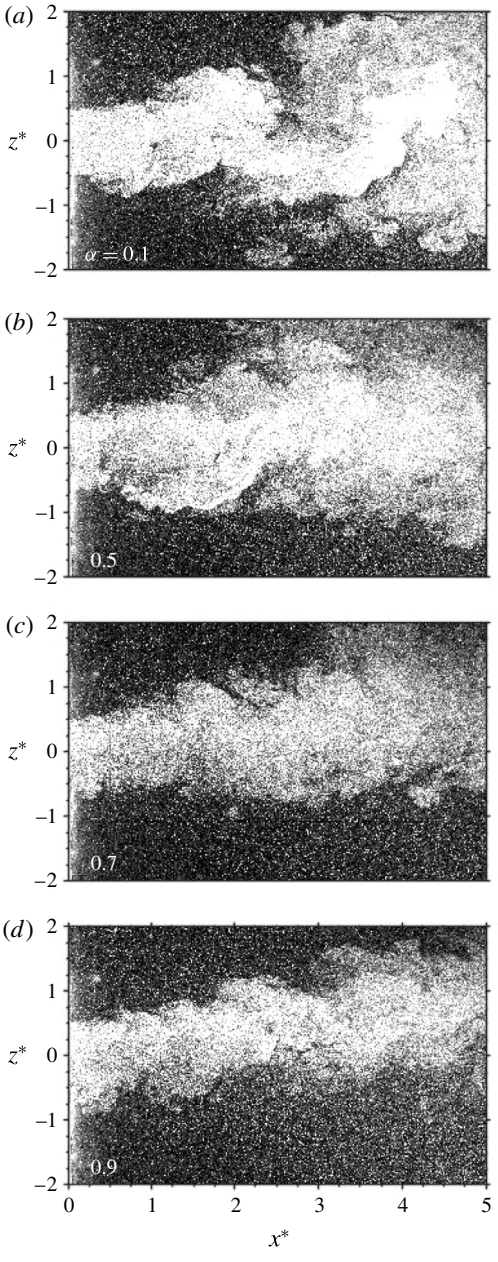


FIGURE 27. Typical flow structures in the injection plane of the jets from flow visualization ($f_e/f_0 = 0.5$, $d/D = 1/20$) corresponding to the ξ value in figure 20: (*a*) $\xi = (\sqrt{MR}/\alpha)(d/D)^n = 1.8$ on curve *B*3; (*b*) 1.0 on *B*2; (*c*) 1.1 on *B*12; (*d*) 1.5 on *B*1.

maximum penetration depth (§ 3). *B*3 is characterized by $\alpha = 0.1$ ($n = 0.25$), where the flow structure experiences a flapping column (figure 27*a*). Physically, the minijet is encountered by a large retardation for $\xi > 1$. For instance, the time-averaged velocity ($\bar{U}_m$) of minijet at $\xi = 1.5$ and $\alpha = 0.1$ is 48 m s^{-1}, but the actual velocity during the

https://doi.org/10.1017/jfm.2018.376 Published online by Cambridge University Press

'on-state' of the minijet exceeds sonic ($\bar{U}_m/\alpha > 340$ m s^{-1}). Evidently, branch $B3$ is in effect associated with partial choking given $\xi > 1$. Branch $B2$ corresponds to the α range of 0.3–0.5 ($n = 0.12$–0.2). The flapping does not occur for $B2$ (figure 27*b*), and hence its maximum K ($= 0.52$ at $\xi = 1.15$) is smaller than that of $B3$. Branches $B1$ and $B12$ correspond to $\alpha = 0.9$ and 0.7, respectively, or the zero retardation effect ($n \approx 0$). In these cases, given $\xi = 1.0$–2.0, the jet column appears deflected, as illustrated in figure 27(*c*,*d*). Note that branch $B12$ is an intermediate branch between $B1$ and $B2$ (figure 22). The deflection angle determined from the time-averaged data of 300 pairs of PIV images (not shown) is approximately 7° (for $B12$, figure 27*c*) and 10° (for $B1$, figure 27*d*) at $\xi \approx 1.0$ and 1.5, respectively. As K is measured on the geometrical jet axis, the stable jet column deflection then yields an artificial increase in the maximum K. As the vectoring angle for $B12$ is smaller than $B1$, the maximum K for $B12$ is smaller than that for $B1$. The phenomenon of jet deflection away from the geometric axis is termed as thrust vectoring. Thrust vectoring has not been observed for jet controlled with two minijets (Davis 1982) or symmetric injection (6 minijets, Seidel *et al.* 2005) since asymmetric excitation is responsible for thrust vectoring (Pack & Seifert 2001). Beyond its maximum, K drops almost linearly with increasing ξ for every branch as the minijet impingement upon the opposite nozzle wall now produces turbulence (figure 5), which may affect adversely the formation and development of organized structures.

Some interesting inferences can be made from (5.2*a*) to (5.2*d*). Firstly, given C_m, f_e/f_0, d/D and α (thus n), ξ may be calculated and hence K can be predicted from the equations. This may have important applications in engineering. Secondly, the required C_m (figure 28*a*) to achieve a pre-specified K can be estimated from (5.2*a*). C_m is a practically important parameter. Following (5.3), we may define a percentage reduction as α reduces, *viz.*

$$\Delta C_{m_\alpha} = 1 - \frac{[C_m]_{0.1\text{–}0.8}}{[C_m]_{0.9}}, \tag{5.6}$$

where subscripts 0.1–0.8 and 0.9 denote α. A large ΔC_{m_α} means a higher control efficiency (figure 28*b*). For example, to achieve a pre-determined $K = 0.3$ for $d/D = 1/40$, C_m required may be calculated from (5.2*a*), which is 0.25 % at $\alpha = 0.1$, 68 % lower than that ($C_m = 0.80$ %) at $\alpha = 0.9$ calculated from (5.6). The result highlights the highly effective entrainment under the unsteady minijet excitation of small α. Lastly, as noted earlier, the required C_m drops as d/D is reduced (figure 28*a*), also implying an improved control efficiency.

6. Conclusions

Experimental study has been carried out to study the manipulation of a turbulent round jet with a single unsteady minijet. Four control parameters, i.e. C_m, f_e/f_0, α and d/D, are examined to understand their influence on the main jet. Extensive measurements are performed in three orthogonal planes of the main jet. The scaling analysis of the jet control is also performed empirically. Following conclusions are drawn from the investigation:

(i) The control performance, as indicated by K, of the manipulated jet strongly depends on C_m, f_e/f_0, α and d/D, i.e. $K = g_1$ (C_m, f_e/f_0, α, d/D). The maximum K occurs in general at $f_e/f_0 = 0.5$ (figure 7), not at 1.0, regardless of d/D, primarily due to jet flapping generated at $f_e/f_0 = 0.5$ but not at $f_e/f_0 = 1.0$.

https://doi.org/10.1017/jfm.2018.376 Published online by Cambridge University Press

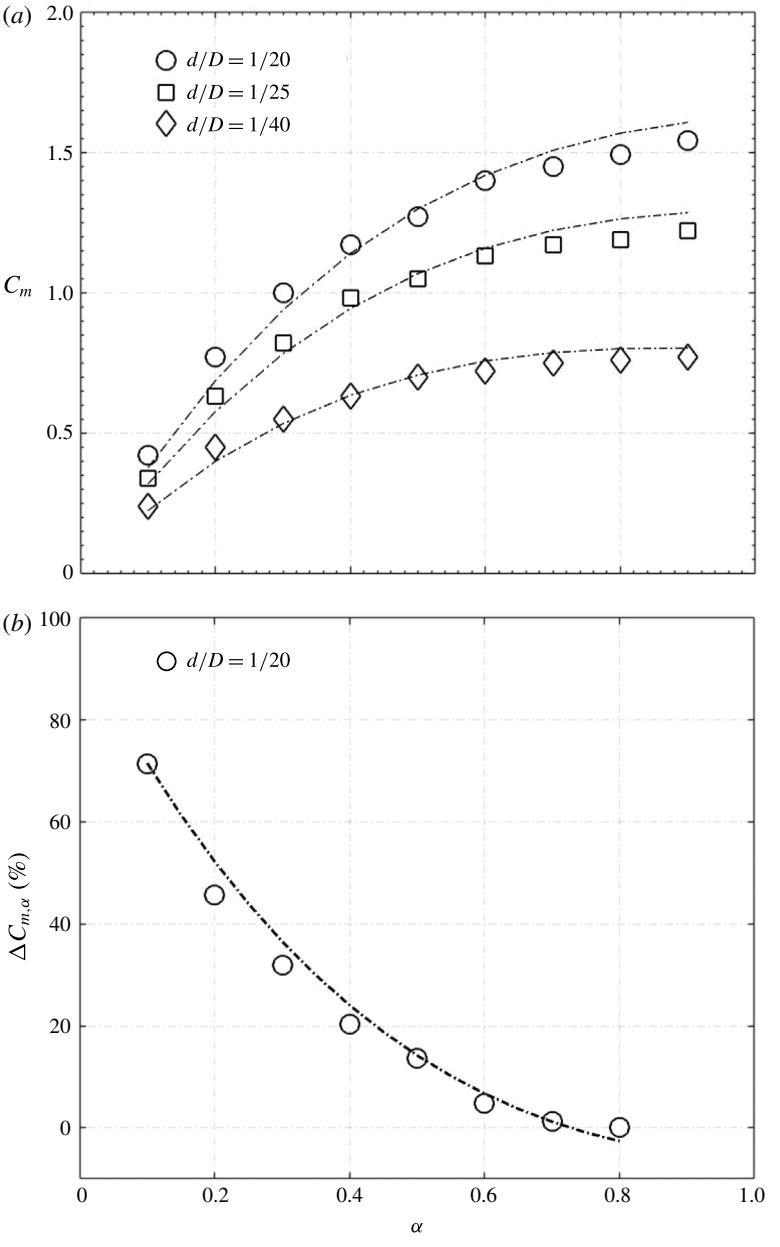


FIGURE 28. Variation of (*a*) C_m and (*b*) $\Delta C_{m,\alpha}$, with α given $\xi = 0.40$ or $K = 0.3$ $(f_e/f_0 = 0.5)$.

Given $f_e/f_0 = 0.5$ and $\alpha = 0.1$–0.9, the variation in K with increasing C_m is characterized by two distinct categories: (i) a rapid rise to a local maximum at $C_m = 2.0\,\%$–$5.0\,\%$ followed by a drop, and (ii) a monotonic growth. The greatly increased K in the first category is largely due to the generation of the flapping motion, while the monotonic rise in K in the second category is caused by the intensified turbulence at higher C_m (Yang & Zhou 2016). The K decreases from

https://doi.org/10.1017/jfm.2018.376 Published online by Cambridge University Press

$\alpha = 0.1$ to 0.9, irrespective of C_m, although the variation is negligibly small beyond $\alpha > 0.7$. It has been found from the flow visualization and spectral phase data that the flapping jet column occurs for $\alpha = 0.1$ and disappears for $\alpha > 0.3$. The smaller d/D is more efficient in enhancing mixing than the larger. Given C_m, the smaller d/D is associated with a larger penetration depth due to the increased injection velocity.

(ii) Empirical scaling analysis has demonstrated that, given a large α say 0.9, the main jet behaves as quasi-steady blowing and the dependence of the measured K on the momentum ratio $\sqrt{MR} = C_m(D/d)$ of the minijet to main jet collapses for various d/D, that is, $\sqrt{MR}$ is the controlling scaling factor. Once α is reduced to below 0.9, K varies with d/D, but the dependence on $\sqrt{MR}$ of the rescaled K, i.e. $K(D/d)^n$, again collapses for various d/D; so does the dependence on f_e/f_0 of $K(D/d)^n$. The power index n is dependent only on α and may be given by $n = -0.31\alpha + 0.28$ for the present flow and control conditions. Thus, $K = g_1$ (C_m, f_e/f_0, α, d/D) is reduced to one similarity parameter, $\xi = (\sqrt{MR}/\alpha)(d/D)^n$, where dimensionless parameters $\sqrt{MR}/\alpha$ and $(D/d)^n$ are physically the momentum per pulse of the minijet and the resistance/retardation to fluid flowing through the minijet orifice, respectively. For $\alpha \geqslant 0.7$, $n \approx 0$, that is, the retardation effect is negligibly small. For unsteady injection, this retardation increases with a decrease in d/D as the C_m required to achieve a pre-determined K is simply governed by $\sqrt{MR}$ or (D/d) for $\alpha \geqslant 0.7$ but $\sqrt{MR}(d/D)^n$ for $\alpha < 0.7$. For example, a decrease in d/D by half results in a decrease in the required C_m by 50 % for $\alpha \geqslant 0.7$ but a decrease in C_m by 40 %, rather than 50 % (figure 23), for $\alpha = 0.1$. The fact that some additional C_m, proportional to $(d/D)^{-n}$, is required to achieve a pre-defined ξ is physically due to the retardation effect.

(iii) The scaling relation branches into four, $B1$, $B2$, $B12$ and $B3$, beyond $\xi > 1.0$. $B1$ corresponds to $\alpha = 0.9$ or above, i.e. the quasi-steady blowing or zero retardation effect ($n = 0$). $B2$ corresponds to $\alpha = 0.3$–0.5 or a moderate retardation ($n = 0.06$–0.20). $B12$ is an intermediate branch between $B1$ and $B2$, corresponding to $\alpha = 0.7$. $B3$ is associated with $\alpha = 0.1$ or a high retardation ($n = 0.25$), under which the minijet is partially choked at $\xi > 1.0$ where C_m is large. There is a considerable difference in the maximum K between the four branches. Branches $B3$ and $B2$ are characterized by flapping and non-flapping jet columns, respectively. It is the flapping motion that is responsible for the larger maximum K of $B3$ than that of $B2$. On the other hand, the jet columns of $B1$ and $B12$ deflect away from the geometric axis, experiencing the thrust vectoring phenomenon. This deflection produces an artificial increase for K and hence their maximum K values exceed those of $B3$ and $B2$.

(iv) The similarity parameter ξ or the effective momentum per pulse of injection may be further interpreted as the effective penetration depth. Given the same $\boldsymbol{\xi}$, the flow structure and its downstream development are essentially the same; for instance, the streamwise variation in the jet mean velocity half-width $z^*_{0.5}$ collapses well over $x^* \approx 0$–5, irrespective of different combinations of C_m and d/D.

(v) Given ξ or K, the required C_m drops as the duty cycle or the minijet injection diameter is reduced, that is, the control efficiency is improved. For example, a 68 % reduction in required C_m is achieved at $\alpha = 0.1$ compared to that at $\alpha = 0.9$, which highlights the highly effective entrainment under the unsteady minijet excitation of small α; a decrease in d/D by half results in a decrease in the

https://doi.org/10.1017/jfm.2018.376 Published online by Cambridge University Press

required C_m by 40 % ($\alpha = 0.1$), that is, the choice of d/D may have an important impact on jet mixing. The penetration depth, flow structure and its downstream development are found to be the same, irrespective of different C_m and d/D, as long as ξ is unchanged. The required momentum ratio or C_m at given d/D and α to achieve a pre-determined ξ or K can be calculated from the scaling relation (figure 22).

Acknowledgements

Y.Z. wishes to acknowledge support given to him from NSFC through grants 11632006 and U1613226 and A.K.P. acknowledges the support from Research Grants Council of Shenzhen Government through grant JCYJ20160531193220561.

Appendix A. Incompressible assumption

To check the validity of incompressible assumption, we compare the $\bar{U}_m$ values estimated using incompressible and compressible equations. $\bar{U}_m$ can be calculated from the equation $\dot{m}_m = \rho_m A_m \bar{U}_m$ given $\dot{m}_m$ and ρ_m, where ρ and A denote the density of the fluid medium (air) and exit area of the minijet, respectively. If the minijet flow is compressible, ρ_m is unknown and hence $\dot{m}_m$ can be rewritten, with ρ_m eliminated, as following (see equation (4.16) in Shapiro 1953),

$$\dot{m}_m = \frac{A_m P_0}{\sqrt{T_0}} \sqrt{\frac{\gamma}{R}} M_m \left(1 + \frac{\gamma - 1}{2} M_m^2\right)^{-((\gamma+1)/(2(\gamma-1)))}, \tag{A 1}$$

where, P_0, T_0, γ, R and M_m represent the stagnation pressure, stagnation temperature for the minijet, specific heat ratio, gas constant and Mach number at the minijet exit, respectively. P_0 is unknown in (A 1), which can be replaced from the following isentropic equation, *viz.*

$$\frac{P_0}{P} = \left(1 + \frac{\gamma - 1}{2} M_m^2\right)^{\gamma/(\gamma-1)}, \tag{A 2}$$

where P is the atmospheric pressure. On rearranging,

$$\dot{m}_m = \frac{A_m P}{\sqrt{T_0}} \sqrt{\frac{\gamma}{R}} M_m \left(1 + \frac{\gamma - 1}{2} M_m^2\right)^{1/2}. \tag{A 3}$$

For a given $\dot{m}_m$, M_m can be calculated from (A 3), noting the predefined '$d = 1$ mm', $p = 1$ atm, $\gamma = 1.4$ and $R = 287$ J kg^{-1} K^{-1}. Then, from isentropic equation,

$$\frac{T_0}{T} = 1 + \frac{\gamma - 1}{2} M_m^2. \tag{A 4}$$

From Mach number relation,

$$\bar{U}_m = M_m \sqrt{\gamma R T}. \tag{A 5}$$

Finally, $\bar{U}_m$ can be determined from (A 5) from the known M_m (A 3) and T (A 4). Note that $T_0 = 298$ K in the settling chamber.

https://doi.org/10.1017/jfm.2018.376 Published online by Cambridge University Press

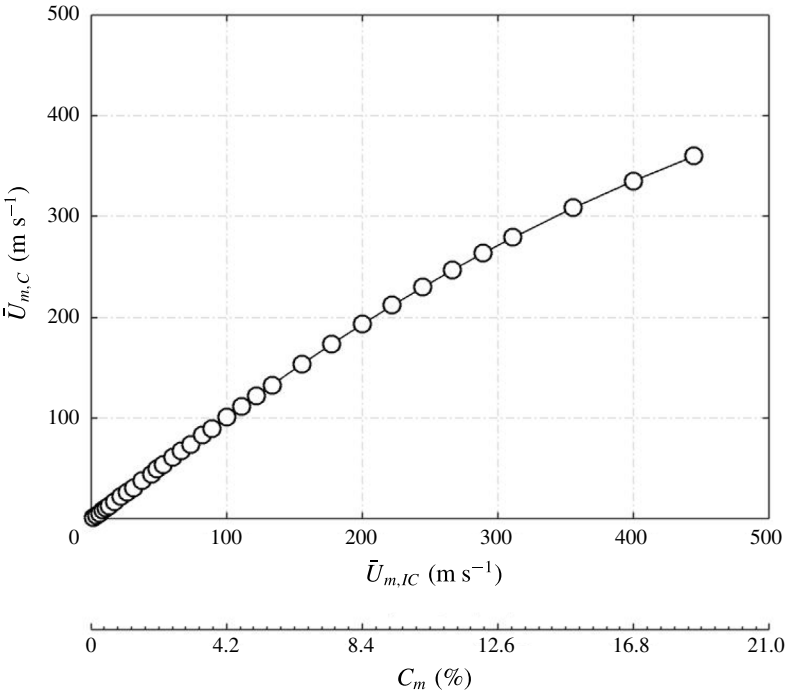


FIGURE 29. Variation in $\bar{U}_m$ with C_m for $d/D = 1/20$.

To determine the error involved in assuming the minijet flow to be incompressible, we calculate $\bar{U}_m$ for incompressible flow and compare it with $\bar{U}_m$ calculated from (A 5).

$$C_m = \frac{\dot{m}_m}{\dot{m}_j} = \frac{\rho_m}{\rho_j}\frac{A_m}{A_j}\frac{\bar{U}_m}{\bar{U}_j}. \tag{A 6}$$

Assuming incompressible flow and rearranging (A 6) yield

$$\bar{U}_m = C_m \left(\frac{D}{d}\right)^2 \bar{U}_j. \tag{A 7}$$

Figure 29 compares $\bar{U}_m$ obtained from the incompressible assumption (A 7) with that from (A 5), where subscripts IC and C denote incompressible and compressible assumptions, respectively. It is evident that for $C_m < 4.2\,\%$ the deviation in $\bar{U}_m$ between the two assumptions is approximately zero. For $4.2\,\% < C_m < 8.2\,\%$, this deviation is no more than $3\,\%$. The present scaling analysis considered for Category I falls within $0 < C_m < 8.2\,\%$. As such, the error associated with the use of equation $MR = \dot{m}_m\bar{U}_m/\dot{m}_j\bar{U}_j = (\dot{m}_m/\dot{m}_j)^2(\rho_m/\rho_j)(A_j/A_m) = C_m^2(D/d)^2$ does not exceed $3\,\%$.

REFERENCES

ALKISLAR, M. B., KROTHAPALLI, A. & BUTLER, G. 2007 The effect of streamwise vortices on the aeroacoustics of a Mach 0.9 jet. *J. Fluid Mech.* **578**, 139–169.

BALL, C. G., FELLOUAH, H. & POLLARD, A. 2012 The flow field in turbulent round free jets. *Prog. Aerosp. Sci.* **50**, 1–26.

https://doi.org/10.1017/jfm.2018.376 Published online by Cambridge University Press

BEHROUZI, P., FENG, T. & MCGUIRK, J. J. 2008 Active flow control of jet mixing using steady and pulsed fluid tabs. *Proc. Inst. Mech. Engrs* **222**, 381–392.

BRADBURY, L. J. S. & KHADEM, A. H. 1975 The distortion of a jet by tabs. *J. Fluid Mech.* **70**, 801–813.

BREIDENTHAL, R. E., TONG, K. O., WONG, G. S., HAMERQUIST, R. D. & LANDRY, P. B. 1985 Turbulent mixing in two-dimensional ducts with transverse jets. *AIAA J.* **21** (11), 1867–1869.

BROWN, G. L. & ROSHKO, A. 1974 On density effects and large scale structures in turbulent mixing layers. *J. Fluid Mech.* **64**, 775–816.

BONS, J. P., SONDERGAARD, R. & RIVIR, R. B. 2001 The fluid dynamics of LPT blade separation control using pulsed jets. *J. Turbomach.* **124** (1), 77–85.

CATTAFESTA, L. N. III & SHEPLAK, M. 2011 Actuators for active flow control. *Annu. Rev. Fluid Mech.* **43**, 247–272.

CHAUVET, N., DECK, S. & JACQUIN, L. 2007 Numerical study of mixing enhancement in a supersonic round jet. *AIAA J.* **45**, 1675–1687.

CHUE, S. H. 1975 Pressure probes for fluid measurement. *Prog. Aerosp. Sci.* **16**, 147–223.

COUSSEMENT, A., GICQUEL, O. & DEGREZ, G. 2012 Large Eddy simulation of pulsed jet in cross flow. *J. Fluid Mech.* **695**, 1–34.

CROW, S. C. & CHAMPAGNE, F. H. 1971 Orderly structure in jet turbulence. *J. Fluid Mech.* **48**, 547–591.

DAVIS, M. 1982 Variable control of jet decay. *AIAA J.* **20**, 606–609.

EDWARDS, A. C., SHERMAN, W. D. & BREIDENTHAL, R. E. 1985 Turbulent mixing in tubes with transverse injection. *AIChE J.* **31**, 516–518.

EROGLU, A. & BREIDENTHAL, R. E. 2001 Structure, penetration, and mixing of pulsed jets in crossflow. *AIAA J.* **39**, 417–423.

FAN, D. W., WU, Z., YANG, H., LI, J. D. & ZHOU, Y. 2017 A modified extremum seeking closed-loop system for jet mixing enhancement. *AIAA J.* **55**, 3891–3902.

FREUND, J. B. & MOIN, P. 2000 Jet mixing enhancement by high-amplitude fluidic actuation. *AIAA J.* **38**, 1863–1870.

GUTMARK, E. & GRINSTEIN, F. 1999 Flow control with noncircular jets. *Annu. Rev. Fluid Mech.* **31**, 239–272.

GUTMARK, E. & HO, C. M. 1983 Preferred modes and the spreading rates of jets. *Phys. Fluids* **26**, 2932–2938.

HERMANSON, J. C., WAHBA, A. & JOHARI, H. 1998 Duty-cycle effects on penetration of fully modulated, turbulent jets in crossflow. *AIAA J.* **36**, 1935–1937.

HO, C. M. & HUANG, L. S. 1982 Subharmonics and vortex merging in mixing layers. *J. Fluid Mech.* **119**, 443–473.

HUANG, H., DABIRI, D. & GHARIB, M. 1997 On errors of digital particle image velocimetry. *Meas. Sci. Technol.* **8**, 1427–1440.

HUANG, J. F., ZHOU, Y. & ZHOU, T. M. 2006 Three-dimensional wake structure measurement using a modified PIV technique. *Exp. Fluids* **40**, 884–896.

HUANG, J. M. & HSIAO, F. B. 1999 On the mode development in the developing region of a plane jet. *Phys. Fluids* **11**, 1847–1857.

HUSSAIN, A. K. M. F. 1986 Coherent structures and turbulence. *J. Fluid Mech.* **173**, 303–356.

HUSAIN, H. S & HUSSAIN, A. K. M. F. 1983 Controlled excitation of elliptic jets. *Phys. Fluids* **26**, 2763–2766.

IBRAHIM, M. K., KUNIMURA, R. & NAKAMURA, Y. 2002 Mixing enhancement of compressible jets by using unsteady microjets as actuators. *AIAA J.* **40**, 681–688.

IIO, S., HIRASHITA, K., KATAYAMA, Y., HANEDA, Y., IKEDA, T. & UCHIYAMA, T. 2013 Jet flapping control with acoustic excitation. *J. Flow Control Meas. Vis.* **1**, 49–56.

JOHARI, H. 2006 Scaling of fully pulsed jets in crossflow. *AIAA J.* **44**, 2719–2725.

JOHARI, H., PACHECO-TOUGAS, M. & HERMANSON, J. 1999 Penetration and mixing of fully modulated turbulent jets in crossflow. *AIAA J.* **37**, 842–850.

KAMRAN, M. A. & MCGUIRK, J. J. 2011 Subsonic jet mixing via active control using steady and pulsed control jets. *AIAA J.* **49**, 712–724.

https://doi.org/10.1017/jfm.2018.376 Published online by Cambridge University Press

KARAGOZIAN, A. R. 2014 The jet in crossflow. *Phys. Fluids* **26**, 1–47.

KNOWLES, K. & SADDINGTON, A. J. 2006 A review of jet mixing enhancement for aircraft propulsion applications. *Proc. Inst. Mech. Engrs* **220**, 103–127.

KUMAR, A. P., VERMA, S. B. & RATHAKRISHNAN, E. 2015 Experimental study of subsonic and sonic jets controlled by air tabs. *J. Propul. Power* **31**, 1473–1481.

LARDEAU, S., LAMBALLAIS, É. & BONNET, J. P. 2002 Direct numerical simulation of a jet controlled by fluid injection. *J. Turbul.* **3**, N2.

MALMSTROM, T. G., KIRKPATRICK, A. T., CHRISTENSEN, B. & KNAPPMILLER, K. D. 1997 Centreline velocity decay measurements in low-velocity axisymmetric jets. *J. Fluid Mech.* **346**, 363–377.

M'CLOSKEY, R. T., KING, J. M., CORTELEZZI, L. & KARAGOZIAN, A. R. 2002 The actively controlled jet in crossflow. *J. Fluid Mech.* **452**, 325–335.

MELLING, A. 1997 Tracer particles and seeding for particle image velocimetry. *Meas. Sci. Technol.* **8**, 1406.

NAMER, I. & OTUGEN, M. V. 1988 Velocity measurements in a plane turbulent air jet at moderate Reynolds numbers. *Exp. Fluids* **6**, 387–399.

NEW, T. H., LIM, T. T. & LUO, S. C. 2006 Effects of jet velocity profiles on a round jet in cross-flow. *Exp. Fluids* **40**, 859–875.

NEW, T. H. & TAY, W. L. 2004. Effects of circumferential microjets on the near-field behavior of a round jet. *AIAA Paper* 2004-092.

PACK, L. G. & SEIFERT, A. 2001 Periodic excitation for jet vectoring and enhanced spreading. *J. Aircraft* **38**, 486–495.

PAREKH, D., KIBENS, V., GLEZER, A., WILTSE, J. & SMITH, D. 1996 Innovative jet flow control: mixing enhancement experiments. *AIAA paper* 96-0308.

PATTENDEN, R. J., TURNOCK, S. R. & ZHANG, X. 2005 Measurements of the flow over a low-aspect-ratio cylinder mounted on a ground plane. *Exp. Fluids* **39**, 10–21.

RAMAN, G. 1997 Using controlled unsteady fluid mass addition to enhance jet mixing. *AIAA J.* **35**, 647–656.

RAMAN, G. & CORNELIUS, D. 1995 Jet mixing control using excitation from miniature oscillating jets. *AIAA J.* **33**, 365–368.

RAMAN, G., HAILYE, M. & RICE, E. J. 1993 Flip–flop jet nozzle extended to supersonic flows. *AIAA J.* **31**, 1028–1035.

ROSHKO, A. 1976 Structure of turbulent shear flows: a new look. *AIAA J.* **14**, 1349–1357.

SAILOR, D. J., ROHLI, D. J. & FU, Q. 1999 Effect of variable duty cycle flow pulsations on heat transfer enhancement for an impinging air jet. *Intl J. Heat Fluid Flow* **20**, 574–580.

SAMIMY, M., KIM, J.-H., KASTNER, J., ADAMOVICH, I. & UTKIN, Y. 2007 Active control of high-speed and high-Reynolds-number jets using plasma actuators. *J. Fluid Mech.* **578**, 305–330.

SAU, R. & MAHESH, K. 2010 Optimization of pulsed jet in crossflow. *J. Fluid Mech.* **653**, 365–390.

SEIDEL, J. F., PAPPART, C., NEW, T. H. & TSAI, H. M. 2005 Effects of multiple radial blowing around a circular jet. *AIAA Paper* 2005-866.

SEIFERT, A., DARABI, A. & WYGANSKI, I. 1996 Delay of airfoil stall by periodic excitation. *J. Aircraft* **33**, 691–698.

SHAPIRO, A. H. 1953 *The Dynamics and Thermodynamics of Compressible Fluid Flow*, vol. 1. Ronald Press.

TAMBURELLO, D. A. & AMITAY, M. 2007 Three-dimensional interactions of a free jet with a perpendicular synthetic jet. *J. Turbul.* **8**, 1–21.

VLASOV, YE. V. & GINEVSKIY, A. S. 1974 Generation and suppression of turbulence in an axisymmetric turbulent jet in the presence of an acoustic influence. *Tech. Rep.* TT F-15, 721. NASA.

WAN, C. & YU, S. C. M. 2013 Numerical investigation of the air tabs technique in jet flow. *J. Propul. Power* **29**, 42–49.

WILTSE, J. M. & GLEZER, A. 1993 Manipulation of free shear flows using piezoelectric actuators. *J. Fluid Mech.* **249**, 261–285.

https://doi.org/10.1017/jfm.2018.376 Published online by Cambridge University Press

WICKERSHAM, P. 2007 Jet mixing enhancement by high amplitude pulse-fluidic actuator. PhD thesis, Georgia Institute of Technology.

YANG, H. 2017 Study of active jet control using unsteady minijets. PhD thesis, Harbin Institute of Technology Shenzhen Graduate School.

YANG, H. & ZHOU, Y. 2016 Axisymmetric jet manipulated using two unsteady minijets. *J. Fluid Mech.* **808**, 362–396.

YANG, H., ZHOU, Y., SO, R. M. C. & LIU, Y. 2016 Turbulent jet manipulation using two unsteady azimuthally separated radial minijets. *Proc. R. Soc. Lond.* A **472**, 20160417.

YU, S., LIM, K., CHAO, W. & GOH, X. 2008 Mixing enhancement in subsonic jet flow using the air-tab technique. *AIAA J.* **46**, 2966–2969.

ZAMAN, K. B. M. Q., BRIDGES, J. E. & HUFF, D. L. 2011 Evolution from 'tabs' to 'chevron technology' – a review. *Intl J. Aeroacoust.* **10**, 685–709.

ZAMAN, K. B. M. Q. & HUSSAIN, A. K. M. F. 1981 Turbulence suppression in free shear flows by controlled excitation. *J. Fluid Mech.* **103**, 133–159.

ZHOU, Y., DU, C., MI, J. & WANG, X. 2012 Turbulent round jet control using two steady minijets. *AIAA J.* **50**, 736–740.

https://doi.org/10.1017/jfm.2018.376 Published online by Cambridge University Press